

Article

CloudSat-Based Assessment of GPM Microwave Imager Snowfall Observation Capabilities

Giulia Panegrossi ^{1,*} , Jean-François Rysman ¹, Daniele Casella ², Anna Cinzia Marra ¹, Paolo Sanò ¹ and Mark S. Kulie ³ 

¹ Institute of Atmospheric Sciences and Climate (ISAC)—National Research Council (CNR), 00133 Rome, Italy; jeanfrancois.rysmann@artov.isac.cnr.it (J.-F.R.); a.marra@isac.cnr.it (A.C.M.); paolo.sano@artov.isac.cnr.it (P.S.)

² SERCO S.p.A., 00044 Frascati, Italy; danielecasellamail@gmail.com

³ Department of Geological & Mining Engineering & Sciences, Michigan Technological University, Houghton, MI 49931, USA; mkulie@mtu.edu

* Correspondence: g.panegrossi@isac.cnr.it; Tel.: +39-06-4993-4274

Received: 12 October 2017; Accepted: 1 December 2017; Published: 6 December 2017

Abstract: The sensitivity of Global Precipitation Measurement (GPM) Microwave Imager (GMI) high-frequency channels to snowfall at higher latitudes (around 60°N/S) is investigated using coincident CloudSat observations. The 166 GHz channel is highlighted throughout the study due to its ice scattering sensitivity and polarization information. The analysis of three case studies evidences the important combined role of total precipitable water (TPW), supercooled cloud water, and background surface composition on the brightness temperature (TB) behavior for different snow-producing clouds. A regression tree statistical analysis applied to the entire GMI-CloudSat snowfall dataset indicates which variables influence the 166 GHz polarization difference (166 Δ TB) and its relation to snowfall. Critical thresholds of various parameters (sea ice concentration (SIC), TPW, ice water path (IWP)) are established for optimal snowfall detection capabilities. The 166 Δ TB can identify snowfall events over land and sea when critical thresholds are exceeded (TPW > 3.6 kg·m⁻², IWP > 0.24 kg·m⁻² over land, and SIC > 57%, TPW > 5.1 kg·m⁻² over sea). The complex combined 166 Δ TB-TB relationship at higher latitudes and the impact of supercooled water vertical distribution are also investigated. The findings presented in this study can be exploited to improve passive microwave snowfall detection algorithms.

Keywords: snowfall detection; GPM; CloudSat; CPR; CALIPSO; high latitudes; passive microwave; remote sensing of precipitation

1. Introduction

Snowfall detection from space using passive microwave (PMW) observations is extremely challenging. Two main obstacles are encountered by PMW snowfall retrieval schemes: (i) the inability to reliably distinguish the respective falling snow and background surface contributions to the upwelling radiation from the earth/atmosphere system [1,2]; and (ii) the quantitative precipitation estimation uncertainties related to varying and ill-constrained ice/snow microphysical properties that obfuscate high microwave frequency ice/snow particle scattering signatures [3]. High latitude surfaces are also frequently (or permanently) snow or ice-covered with elevated and variable surface emissivities [4,5], thus rendering the solid precipitation contribution to upwelling microwave radiation difficult to isolate from the surface contribution. This issue is further magnified by the relatively subtle PMW signal associated with low precipitation rates [6]. Various studies have shown that extremely light snowfall rates dominate the snowfall rate distribution at higher latitudes [7–9].

Microwave sensors with high-frequency channel diversity offer a unique opportunity for significant advances in surface snowfall retrievals. It is worth noting that the lengthy legacy microwave

radiometer imager precipitation data record collected by such instruments as the Special Sensor Microwave Imager (SSM/I), the Tropical Rainfall Measuring Mission (TRMM) Microwave Imager (TMI), and the Advanced Microwave Scanning Radiometer-EOS (AMSR-E) included microwave channels up to 85/89 GHz. The 85/89 GHz channels are considered high-frequency microwave channels with demonstrated ice scattering sensitivity associated with tropical and mid-latitude rain events [10,11]. These channels on microwave imagers that employ fixed oblique observation angles can be especially useful for oceanic precipitation rate retrievals by exploiting high-frequency polarization signals. Tools that exploit polarization information have been developed to isolate the ice scattering brightness temperature (TB) signature at higher microwave frequencies from highly polarized oceanic background (e.g., the scattering index in the study by Petty [12]). The 85/89 GHz channels, however, are too sensitive to the surface at higher latitudes, where the atmosphere opacity is lower, for consistently effective snowfall retrieval, especially over land surfaces [1]. This is why higher frequency “window” channels located in 150–170 GHz range, combined with observations utilizing gaseous absorption features between 100 and 200 GHz, are now privileged for snowfall detection since they respond more effectively to ice microphysics compared to 85/89 GHz channels [3,7,13,14]. More importantly, these higher frequency channels—including the so-called “window” channels—are less prone to surface effects because the opacity (transmissivity) of the atmosphere increases (decreases) as the microwave frequency increases (due to water vapor continuum or oxygen absorption) [15]. In dry conditions, however, the contribution of the surface to the upwelling radiation at these frequencies can be quite significant. Current microwave imagers such as the Global Precipitation Measurement (GPM) Microwave Imager (GMI), combination microwave imager/sounders (e.g., Special Sensor Microwave Imager and Sounder (SSMIS)), and microwave sounders (e.g., Advanced Technology Microwave Sounder (ATMS)) offer high-frequency channel assortment that can be used for snowfall detection and quantitative precipitation retrievals.

Theoretical modeling studies demonstrate the potential of high-frequency channel combinations for snowfall detection purposes [16,17]. While oceanic snowfall rate estimation using high-frequency channels should hypothetically be a tractable retrieval scenario due to a fairly well-behaved and understood surface background, the results by Skofronick-Jackson and Johnson [1] indicate complexities over land surfaces. They demonstrated that higher frequencies (e.g., 166 GHz and 183.3 GHz channels) are more sensitive to frozen hydrometeor scattering and partially mask the surface contribution, but with varying degrees of sensitivity depending on the ice water path and atmospheric moisture profile associated with each snowfall regime. They also highlight the difficulties associated with isolating the snowfall signal at higher microwave frequencies due to complex interaction between surface and atmospheric features that determine the multi-frequency TB signal. Recent work by Ebtehaj and Kummerow [18] using GMI data, however, illustrates that snowfall detection may be possible over land with no snow cover by using combined 10 and 166 GHz horizontal polarization channel information, while 89 GHz horizontal polarization observations provide crucial information for snow-covered surfaces.

Other studies have been carried out to analyze snow scattering signals and the effect of snow particle orientation on polarization differences observed with a ground-based radiometer [19,20]. In the work by Kneifel et al. [19], a significant TB enhancement in ground-based measurements at 90 and 150 GHz is observed in presence of snowfall, due to the large amounts of liquid water and to the presence of supercooled droplets often found for the snowfall cases analyzed. The study by Xie et al. [20] shows that the polarization difference at 150 GHz can be explained by the occurrence of oriented snow particles, and that while high snow water path enhances polarization differences, the presence of supercooled water damps the polarization differences, and enhances the TBs. These studies support the potential role of polarization measurements for improved retrievals of snowfall microphysical parameters, and the importance of accurate modeling of the radiative properties of supercooled water for snowfall retrieval algorithms using high microwave frequencies. Moreover, Kneifel et al. [19] evidenced the need of studies on the use of passive measurements at frequencies

higher than 150 GHz combined with radar systems (above 35 GHz) to test their potential for snowfall detection and retrievals.

The application of high-frequency channels (e.g., 150 and 183.3 GHz)—more specifically, using TB differences from channel pairs with weighting functions that peak at different atmospheric levels—has also been shown in proof-of-concept snowfall detection studies and snowfall product development [6,21–23]. For example, the work by Noh et al. [23] illustrates United States Laurentian Great Lakes snowfall retrieval potential using previous generation operational microwave sounder data from the Advanced Microwave Sounding Unit (AMSU-B). They noted generally positive results, especially in the early winter season when sustained ground snow cover is limited. In later winter months, however, snowfall retrievals using sounding channels were susceptible to snow-covered ground contamination. Enhanced screening methods that account for seasonal surface differences can significantly reduce false detections [6].

High-frequency microwave channels and surface effects are important factors to consider for the current flagship GPM spaceborne mission. The Goddard Profiling algorithm (GPROF) used for GMI precipitation retrievals recognizes the complications associated with distinctive surface emissivities associated with different surface types [24]. For a given GMI observation, the GPROF retrieval scheme restricts its a priori database search, whereby the observation TB vector is optimally matched to a database TB member that minimizes the multi-frequency TB difference. This a priori database search restriction is limited to similar surface classes and environments (e.g., 2 m temperature (T_{2m}) and total precipitable water (TPW)) as the GMI observation, thus reducing computational time and constraining retrieval possibilities to consider only similar surface types. GPROF snowfall retrieval efficacy remains an active research topic, but studies that systematically assess the information contained in various GMI channel combinations for snowfall detection have been undertaken in recent years using spaceborne radar observations to identify snowfall events globally. For instance, in the work by You et al. [2], a coincident GMI and GPM Dual-frequency Precipitation Radar (DPR) database is analyzed to determine optimal channel combinations for snowfall detection over land. Low frequency channels obviously demonstrate little information due to a weak ice scattering response. Including high-frequency channels near the 183.3 GHz water vapor absorption line contributes valuable information, but adding the 166 GHz channel to a multi-frequency channel combination is deemed optimal for snowfall detection using a GMI-like sensor. The 166 GHz channel amplifies ice/snow scattering sensitivity lower in the atmosphere, yet appropriately dampens surface influences and increases snowfall detection statistics when compared to radar-derived snow/no-snow statistics. The possible combination of high-frequency microwave channel responses to different snowfall scenarios, however, deserves further investigative attention.

The importance of high-frequency microwave radiometer observations to better understand ice scattering signatures is further illustrated by Gong and Wu [25], whereby systematic polarized high-frequency signatures are associated with cloudy GMI observations on a global scale. In the work by Gong and Wu [25], it is evidenced that the 89 and 166 GHz polarimetric measurements contain ample information regarding frozen particle habit and orientation. The TB differences (ΔTB) between vertically (V-pol) and horizontally (H-pol) polarized 89 and 166 GHz channel observations are found to be positive, with a distinctive bell-shaped ΔTB curve as a function of V-pol TB that peaks near 10 K for both channels. The ΔTB values are positive because of stronger H-pol extinction under cloudy conditions that may contain significant columnar liquid water and ice paths. The study by Gong and Wu [25], however, notes that cold-season high latitude ΔTB -TB relationships are more complex than the generally invariant low latitude ΔTB -TB relationships. This ΔTB -TB latitudinal discrepancy is most likely related to lower water vapor contents in winter atmospheres at higher latitudes, thus allowing surface influences to complicate the ΔTB signal. Conversely, the ΔTB signal can be dampened at lower latitudes due to elevated TPW amounts. The study by Gong and Wu [25] motivates the need to investigate ΔTB -TB relationships at higher latitudes, especially 166 GHz (V-H)

TB differences (hereafter 166 Δ TB) behavior in the presence of surface snowfall observed by radar with increased sensitivity compared to the DPR.

This study therefore illustrates snowfall signatures over different surface classifications using GMI channel combinations and coincident CloudSat snowfall retrievals. CloudSat sensitive Cloud Profiling Radar (CPR) has proved extremely valuable for global snowfall research [7–9,26,27]. Combined GMI and CloudSat observations can be exploited to study radiometric signals associated with a broader range of the snowfall rate spectrum compared to the GPM DPR since the effective \sim 12 dBZ GPM DPR sensitivity threshold limits its effectiveness to detect lighter snowfall events [28].

Similarly to You et al. [2], this study characterizes GMI snowfall detection capabilities over different surface types by focusing exclusively on high-frequency microwave signatures, with special attention dedicated to the 166 GHz channel. The 166 GHz channel is specifically highlighted for two reasons: (1) while numerous previous studies have thoroughly studied 183 GHz channels for surface snowfall applications [6,21–23], the GMI is the first sensor to employ the 166 GHz channel, and the 166 GHz observational signal in the presence of surface snowfall warrants further investigation; and (2) the 166 GHz channel has been shown to provide impactful information content compared to other high-frequency channels [2]. Additionally, previous studies that highlight 166 GHz GMI observations [2,25] did not employ a highly sensitive radar like CloudSat CPR to effectively observe surface snowfall events with lower snowfall rates.

This study first illustrates case study analyses from a matched GMI-CPR dataset that provides instructive insights to highlight widely varying GMI multi-frequency signals associated with different snowfall types. This is believed to be the first exhaustive GMI TB analysis for varied snowfall events, using CloudSat products to augment the GMI observations. The case study results are followed by an aggregated TB response analysis of the entire GMI-CPR dataset aimed at showing the behavior of GMI 166 GHz channels in presence of snowfall under different environmental conditions. In addition, the study exploits CloudSat products to investigate the impact of supercooled cloud droplets on the GMI observations of snowfall in relation to the environmental conditions and cloud characteristics. The ultimate goal of this study is to provide guidelines derived from the complex relations between GMI observations and snowfall at higher latitudes to be exploited in the development of a snowfall detection algorithm for current and future microwave radiometers. Section 2 provides background information on GMI and CloudSat, on the products used in this study, and on the methodology used to build the GMI-CPR coincidence dataset. Section 3 illustrates the GMI high-frequency sensitivity to snowfall for three different case studies and presents the results of the analysis for the entire GMI/CloudSat dataset. Section 4 is dedicated to the discussion of the main results, and Section 5 to the conclusions.

2. Methodology: GMI-CPR Dataset Description

This study is based on the use of co-located observations by the CPR on board the CloudSat and by the GMI on board the NASA/JAXA GPM Core Observatory. CloudSat has been operational since 2006 as part of the Afternoon Constellation (A-Train) [29] of independent satellites flying in a formation pattern, and it follows a near-polar orbit (maximum latitude near 82°) with a 16-day overpass revisit cycle. Since 2011 CPR operates in daylight-only mode due to a battery anomaly. CloudSat has provided valuable data for the precipitation remote sensing community, especially as the first spaceborne radar to provide observations at higher latitude. The near global coverage (up to $\sim 82^\circ$ latitude) and high CPR sensitivity (\sim –28 dBZ) make it very suitable for snowfall-related research [7–9,27,30–32]. The CPR nominal footprint size is \sim 1.5 km with \sim 480 m native vertical range gates in each reflectivity profile collected over a 0.16 s integration time interval. Due to oversampling, CloudSat products are available at \sim 240 m vertical intervals.

The GMI is the most advanced microwave conically scanning radiometer in space, in terms of both channel frequency assortment and spatial resolution. It offers the most appropriate set of microwave frequencies for precipitation retrieval, with 10 dual-polarization window channels from 10 GHz to

166 GHz, and three single-polarization water vapor absorption channels (at 23.8 GHz and two at 183.3 ± 3 GHz, and 183.3 ± 7 GHz). Moreover, GMI provides PMW measurements on a 904 km wide swath at the highest available spatial resolution, ranging from $4.4 \text{ km} \times 7.2 \text{ km}$ at the high-frequency channels (>89 GHz), to $19 \text{ km} \times 32 \text{ km}$ at 10 GHz.

The GMI-CPR coincidence dataset is built starting from the NASA 2B-CSATGPM product of coincident CloudSat/GPM observations [33], made available through the NASA Precipitation Processing System (PPS), within the Precipitation Measurement Missions (PMM) Research Program. This product is made of coincident segments of CPR co-located reflectivities and GMI TBs within a time interval of 15 min or less. For the pixels located within GPM DPR swaths, centered in the GMI swath (245 km and 120 km wide for the Ku- and Ka-band radar, respectively) the dataset stores DPR reflectivity profiles (measured and corrected). The GMI-CPR database used in this study includes all coincident observations available from March 2014 through the end of May 2016 (no CPR snowfall products were available after this date at the time this study was carried out).

Additional GPM, CloudSat products and ancillary data have been added to the initial dataset for this study in view of future further applications. Precipitation profiles, surface precipitation variables from the NASA 2A-GPROF [24], 2B-CMB products (V4 and V5) [34] and the JAXA GPM 2A-DPR (V4 and V5) [35] have been included in the dataset. In addition, the CloudSat 2C-SNOW-PROFILE (hereafter, 2C-SNOW), used extensively in this study, provides profiles of instantaneous liquid equivalent surface snowfall rate retrievals based on CloudSat orbital swath data. The 2C-SNOW product uses an optimal estimation procedure to extract snowfall rate from W-band radar reflectivity values, using a priori snow microphysical properties to constrain snowfall rate retrievals [36,37]. It is worth noting that 2C-SNOW surface snowfall rate (and associated SWC profile) is computed only for CPR profiles where the 2C-PRECIP CPR product indicates surface snow probable or certain, or if estimated liquid fraction is $<10\%$ (dry snow). These conditions are defined by considering interpolated ECMWF model temperature profiles at the near-surface clutter-free bin, and therefore are subject to the uncertainty of the model and to the ground clutter conditions (see also Casella et al. [28]). Moreover, the SWC is available only at or above the first clutter-free bin and the retrieval is provided only if the equivalent radar reflectivity factor at the first clutter-free bin is above -15 dBZ. Numerous studies have demonstrated that the CPR snowfall rates are possibly biased under different meteorological or geographical circumstances [38,39]. Exhaustive 2C-SNOW algorithm descriptions are also provided by Kulie et al. [9] and Behrangi et al. [27]. All coincident segments for which the 2C-SNOW provides a valid near-surface snowfall rate (at least in some part of the segment) have been selected for the snowfall-only dataset used in this study. In the GMI-CPR dataset used in this study, all snow related variables (i.e., snow water content (SWC), snow water path (SWP)) refer to falling snow, i.e., CPR profiles with 2C-SNOW surface snowfall rate larger than $0.0 \text{ mm} \cdot \text{h}^{-1}$.

Another product added to the original 2B-CSATGPM dataset is the CloudSat DARDAR (liDAR + raDAR) product. It is derived from combined CPR and CALIPSO lidar measurements using a variational approach [40,41]. The DARDAR product supplies the following ice cloud property retrievals: ice water content (IWC), ice particle effective radius, and extinction. These ice properties are provided with a vertical (horizontal) resolution of 60 m (1.7 km). The DARDAR product also provides the predominant particle phase/microphysics composition or constituent classification of each vertical bin in the following 11 classes: ground, unknown, clear, ice, ice and supercooled water, liquid warm, supercooled water, rain, aerosol, possible insect, or stratospheric feature. The assessment of the quality of DARDAR product performed by Hiley et al. [38] and Chen et al. [39] against real and simulated ice profile, shows that DARDAR tends to overestimate IWC (up to 30–40% depending of the altitude of the ice). Hereafter, all ice related variables (i.e., ice water content (IWC), or ice water path (IWP)) will refer to the DARDAR product cloud ice, which includes upper level clouds, thin ice clouds, as well as falling snow.

In addition, ancillary daily snow cover fraction (MOD10C1 from MODIS [42]) and sea-ice concentration (Arctic and Antarctic Sea-ice concentration (ASI) product from AMSR2 [43]), both

at 0.05° , have been added to the dataset. It is worth noting, however, that the MODIS snow cover fraction data are not available for most winter cases, occurring in the dark seasons of the northern and southern hemispheres. Due to this limitation, we have not used the MODIS snow cover information in this study. Note that the percentage of data points characterized by a cold background surface ($T_{2m} < 270$ K) is 88%. This indicates that most of land pixels in the dataset are likely frozen or snow covered. Table 1 provides a list of all products available in the dataset built from coincident GMI/CloudSat observations (March 2014–May 2016), and the main variables used specifically in this study.

Table 1. List of products available in the dataset built from coincident GMI/CloudSat observations (10 March 2014–31 May 2016) and list of the main variables used in this study.

Source	Sensor/Model	Product	Main Variables
GPM	GMI	1C-R V5A	Brightness temperatures (TBs) (K)
GPM	GMI	GPROF V4 and V5	Surface precipitation rate ($\text{mm}\cdot\text{h}^{-1}$) Liquid fraction (V4) (%) Frozen precipitation rate (V5) ($\text{mm}\cdot\text{h}^{-1}$)
CloudSat	CPR	2C-SNOW-PROFILE V4	Equivalent radar reflectivity factor (Z) (dBZ) Snow water content (SWC) ($\text{kg}\cdot\text{m}^{-3}$) Surface snowfall rate ($\text{mm}\cdot\text{h}^{-1}$)
CloudSat	CPR	2C-PRECIP-COLUMN V4	Surface precipitation rate ($\text{mm}\cdot\text{h}^{-1}$) Liquid fraction (%)
CloudSat	CPR	2B-CLOUD-CLASS V4	Surface type Cloud type
CloudSat	ECMWF	ECMWF-AUX V4	2 m temperature (T_{2m}) (K) Surface pressure (hPa) Total precipitable water (TPW) ($\text{kg}\cdot\text{m}^{-2}$)
Icare/University of Lille 1	CALIPSO/CPR	DARDAR	Ice water content (IWC) ($\text{kg}\cdot\text{m}^{-3}$) Phase/microphysics classes
University of Bremen	AMSR2	ASI	Daily sea-ice concentration (%)

In the original GMI-CPR dataset, CPR products are kept at their native resolution while the GPM data (e.g., GMI TBs), ECMWF auxiliary variables, and surface variables, are mapped to the CPR swath using a nearest neighbor approach. In this study (except for the case study analysis in Section 3.1), in order to have a one-to-one correspondence between the GPM and the CloudSat data, a mean CPR profile (and surface snowfall rate) is computed and associated to each GMI pixel (i.e., TB vector) along the CPR swath, by averaging all CPR profiles associated with the same GMI pixel. The final GMI-CPR global dataset consists of 529,350 coincident pixels at GMI high-frequency channel resolution (~ 5 km), with 48,194 snowfall coincident pixels. Figure 1 shows the global distribution of snowfall elements in the GMI-CPR coincidence dataset. Each snowfall occurrence is defined by the non-zero mean surface snowfall rate computed from the 2C-SNOW profiles associated with a GMI TB vector. As evidenced in Turk [33], the largest number of occurrences is found around 60°N and 60°S . It is worth noting that the highest latitude in the GMI/CPR dataset is 69°N/S .

This study investigates GMI high-frequency ΔTB signals in the presence of snowfall under different environmental conditions at higher latitudes benefiting from the high number of concurrent GPM and CloudSat overpasses in these regions. Ambient atmospheric water vapor content and cloud microphysical properties are also combined with surface information using a novel decision tree approach to quantify 166 GHz TB responses over different surface types.

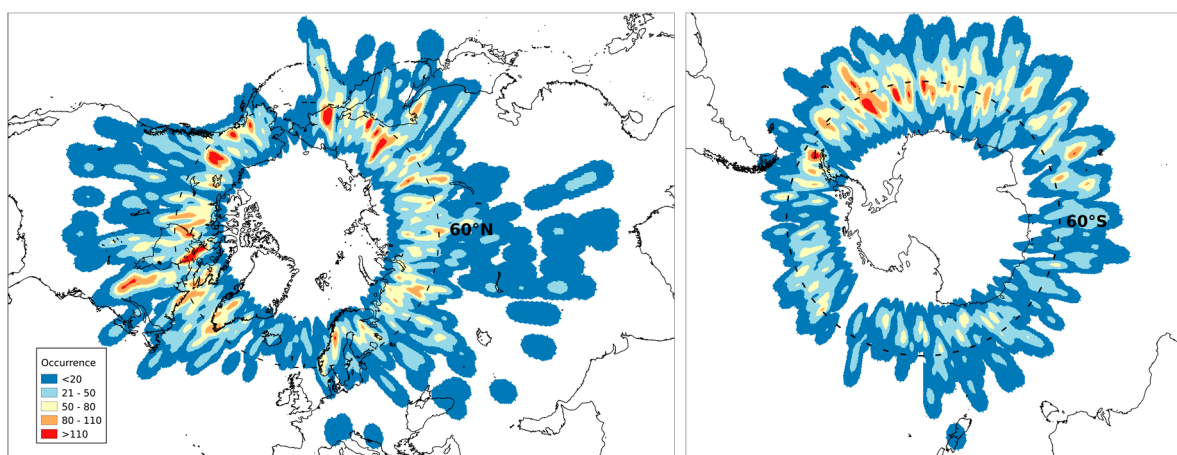


Figure 1. Global distribution of snowfall elements in the GMI-CPR coincidence dataset (March 2014–May 2016). The two panels show the number of occurrences of snowfall elements (indicated by the colors) in the: Northern hemisphere (**left**); and Southern hemisphere (**right**).

3. Results

3.1. Case Studies

Three main case studies that are part of the combined GMI-CPR snowfall dataset are analyzed. One describes an intense, widespread frontal snowfall event, the second an orographic snowfall event, and finally an extensive, deep synoptic snowfall case over the Labrador Sea. The original 2B-CSATGPM dataset is used for the case study analysis, with CPR products at their native resolution, and all other variables mapped to the CPR pixel positions along the swath. Therefore, replications of the same TB values associated with different, adjacent CPR pixels along the CPR orbital swath may be found.

3.1.1. Case 1: Intense Snowfall Event on 30 April 2014

This widespread frontal snowfall event in Eastern Russia on 30 April 2014 was first highlighted from a combined CPR and DPR perspective in Casella et al. [28]. Maximum cloud top heights reach ~8 km in the central portions of this CloudSat overpass segment, with lower snow-producing clouds located on the fringes of this system. A separate snowfall event with cloud top heights near ~5 km is also associated with surface snowfall in the far north and east segment of this overpass (Figure 2a top panel). The highest radar reflectivities are ~15 dBZ in the most intense central snowfall regions (Sector III), while reflectivities are much lower in both the shallow fringe central snowfall zones (Sector II) and the snowfall event located to the north and east (Sector I). SWC retrievals from the CloudSat 2C-SNOW product exceed $5 \times 10^{-4} \text{ kg}\cdot\text{m}^{-3}$ up to the ~5 km level in the most intense precipitation cores, but SWC values do not exceed $2 \times 10^{-4} \text{ kg}\cdot\text{m}^{-3}$ in the other surface snowfall cloud structures. Near surface snowfall rates also exceed $2 \text{ mm}\cdot\text{h}^{-1}$ in the most intense precipitation regions of this event. It is worth noting that, as evidenced in the second panel of Figure 2a, 2C-SNOW SWC is available only above the first clutter-free bin which changes depending on the background surface (higher for snow cover and sea ice, and lower over ocean). Therefore, CPR may miss the snowfall in the first 1000–1500 m above the surface (see also Milani et al. [32]). For example, for the weaker cloud north of 64°N (Sector I), the SWC is not available at the lower levels. This might lead to underestimations in the SWP and surface snowfall rate estimates. An elevated non-precipitating cloud structure is located to the south and west, with cloud top (base) values near 10 (5) km. Maximum reflectivities associated with this cloud approach 10 dBZ near the cloud base.

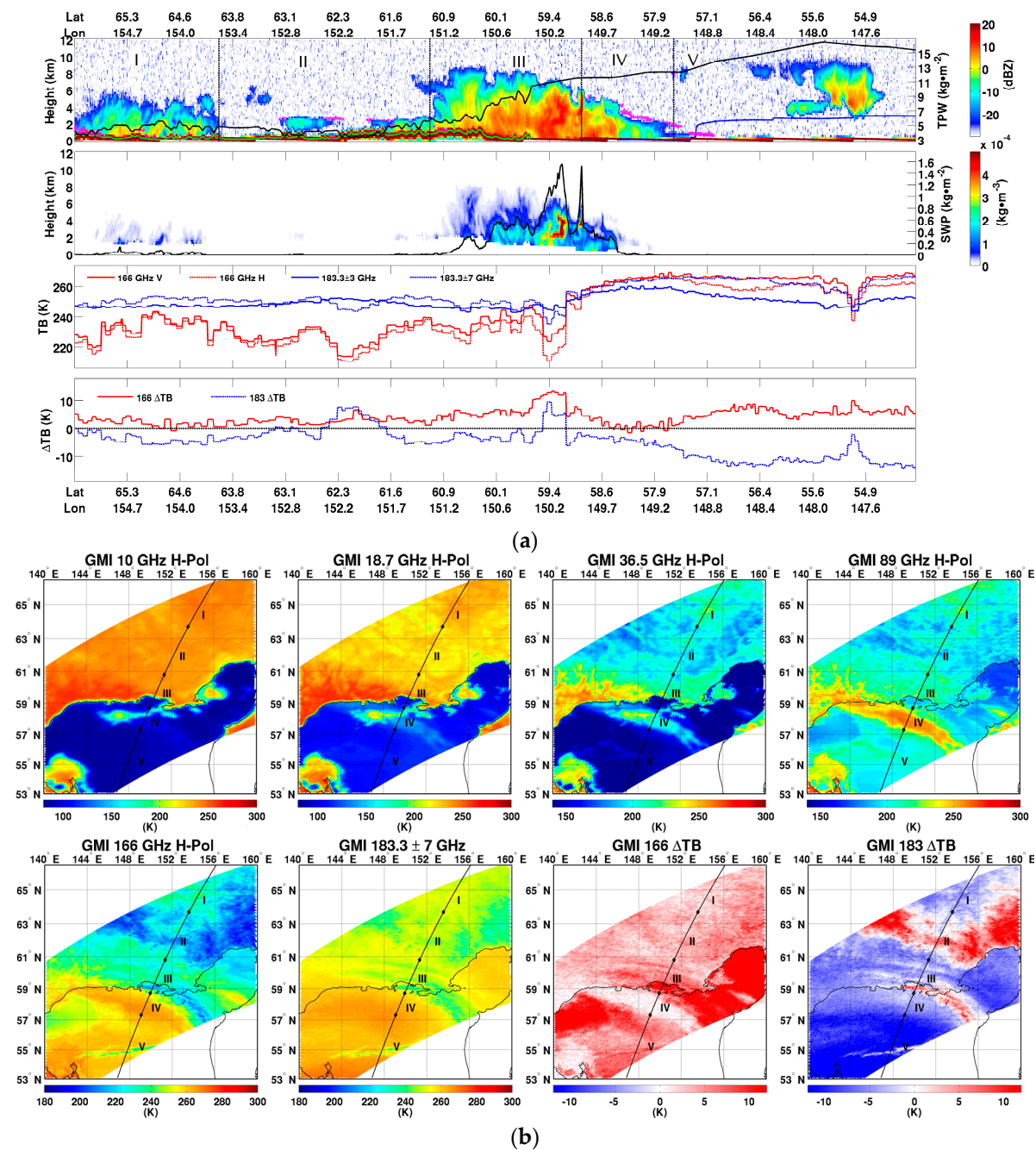


Figure 2. Snowfall event on 30 April 2014. (a) From top to bottom, the first panel shows height-lat/lon imagery of Cloud Profiling Radar (CPR) reflectivity (color bar, in dBZ), the freezing level height (blue curve), and total precipitable water (TPW) (black curve, with values provided on the right-hand side y-axis), along the CloudSat track. In this panel, cloud layers where the DARDAR product identifies supercooled droplets are superimposed and shown in magenta. Second panel shows height-lat/lon imagery of 2C-SNOW snow water content (SWC) (color bar, in kg m^{-3}) and the snow water path (SWP) (black curve, with values provided on right-hand side y-axis). The third panel shows the GMI brightness temperatures (TBs) closest to each CPR pixel along the CloudSat track at 166 GHz (V and H polarization, in red), 183.3 \pm 3 GHz and 183.3 \pm 7 GHz (in blue). Bottom panel shows GMI TB difference (ΔTB) at 166 GHz (V-H, in red), and for the two 183.3 GHz channels (in blue). In the top panel, vertical lines delineate different Sectors (I to V) identified in the discussion (see text for details). (b) GMI TB imagery: top row from left, 10, 18.7, 36.5, and 89 (H-pol) channels; bottom row from left: 166 (H-pol) and 183.3 \pm 7 channels, ΔTB at 166 GHz (V pol–H pol) and at 183.3 GHz (183.3 \pm 3 GHz–183.3 \pm 7 GHz). The black line segment in each panel shows the CloudSat track. The sectors (I to V) identified in the discussion are also indicated (see text for details).

This particular case is interesting to analyze since it exhibits a land-to-ocean transition (59.6°N–150.3°E), with extremely dry TPW values near $\sim 2 \text{ kg}\cdot\text{m}^{-2}$ in the north sector of the scene increasing to over $15 \text{ kg}\cdot\text{m}^{-2}$ in the southern sector (Figure 2a, top panel). A particularly significant TPW change is observed south of 59°N, indicating a distinct frontal structure evidenced also by the surface pressure field (not shown) (note the $183.3 \pm 3 \text{ GHz}$ response to this TPW gradient). Land surfaces are very likely snow covered at this latitude.

Note that, in Casella et al. [28], the DPR Ku uncorrected reflectivity profiles reveal that most of the event north of 59.5° latitude and at higher altitudes is missed by the DPR due to the degraded radar sensitivity compared to the CPR. Moreover, Casella et al. [28] show that DPR Ku uncorrected reflectivity displays some structure below $\sim 4 \text{ km}$ in the deeper snowfall segment of this event between $\sim 58.8^\circ\text{N}$ and 59.5°N .

In the deeper snowfall segments (Sector III), 166 GHz and $183 \pm 7 \text{ GHz}$ TBs show some sensitivity to columnar ice content scattering effects that produce decreasing TBs (i.e., $\sim 15\text{--}20 \text{ K}$ decrease in 166 GHz TBs compared to surrounding regions). In this segment, the 166 ΔTB also show a polarization increase corresponding to the deeper and most intense clouds (as already noted by Xie et al. [20]). This 166 ΔTB feature is correlated to the 183 GHz TB difference ($183.3 \pm 3 \text{ GHz TB} - 183.3 \pm 7 \text{ GHz TB}$, hereafter 183 ΔTB) increase.

In correspondence of the weaker or shallower snow clouds (Sector I and II, north of 60°N), 166 GHz TBs are higher than in the cloud-free regions, where the low TBs (between 210 K and 220 K) are due to the very low water vapor emission ($\text{TPW} < 2 \text{ kg}\cdot\text{m}^{-2}$) over a radiatively cold (likely snow-covered) background (as noted by Ebtehaj and Kummerow [18]). The relatively warmer TBs at 166 GHz in correspondence of the snowfall in these regions are also due to another important effect. TBs at 166 GHz typically decrease due to scattering by sufficient columnar ice content, but this case highlights the sensitivity of 166 GHz to supercooled cloud liquid water. The presence of supercooled water near cloud tops in these shallow clouds has been verified using the CloudSat CPR/CALIPSO DARDAR product as shown in Figure 2a (magenta color layers in the top panel). In the work by Liu and Seo [44], similar TB increases was noted due to cloud liquid water that often mask frozen hydrometeor scattering effects and further complicate high microwave frequency TB signatures associated with snowfall events.

Moving south from 59°N (Sector IV and V), the 166 GHz and 183 GHz TBs progressively increase due to the atmospheric water vapor gradient. Atmospheric temperatures also increase further south (note the abrupt freezing level height increase around 57°N). This water vapor effect dampens the ice scattering effects due to the shallower and weaker portion of the clouds south of 58.6°N (Sector IV), where CPR shows lower reflectivity values ($< 0 \text{ dBZ}$) and shallow surface snowfall structures (according to the 2C-SNOW product). TBs at high frequencies (166 GHz and above) are not affected by such structures because of the water vapor dampening effect (where $\text{TPW} > 10 \text{ kg}\cdot\text{m}^{-2}$), as the 166 GHz weighting function peaks at higher levels with respect to the shallow clouds. The CPR/CALIPSO DARDAR product indicates the presence of supercooled cloud liquid water droplets in the upper cloud layers (Sector IV, magenta layers). The effect of the emission by supercooled droplets is evident at 89 GHz (Figure 2b, top-right panel), while it is not visible at 166 GHz likely because of the stronger emission signal by the water vapor at this frequency. Moreover, 166 ΔTB approaches 0 K because of the depolarization effect of the cloud droplets. In this region (south of 58.6°N, and between 148°E and 152°E), Figure 2b shows faint warming signatures also at low frequencies ($< 37 \text{ GHz}$) with respect to the radiatively cold oceanic surface background, thus indicating the presence of melting snow or drizzle at very low levels. At 10 GHz and 18.7 GHz frequencies, the emission signal is more evident west of 148°E, where it is very likely associated with predominantly liquid precipitation.

The high-frequency channels show sensitivity to the deep cloud with reflectivity exceeding 10 dBZ above 5 km (in Sector II), or in correspondence of the upper level cloud southward of 55.6°N (Sector V). It is also worth mentioning the significant 183 ΔTB (and to a less extent 166 ΔTB) signature associated with this cloud. This very distinctive feature highlights another issue— ΔTB may not be

always linked to surface precipitation: at 183.3 GHz, the cloud may be optically thick from an ice extinction/scattering perspective, yet not deep enough to significantly affect 183.3 ± 3 GHz TBs. At 166 GHz, non-precipitating ice clouds with reflectivity around 5–10 dBZ peaking at high levels (relative to the weighting function), may show significant polarization.

3.1.2. Case 2: Orographic Precipitation Event on 14 December 2014

A coastal orographic snowfall event near and over Alaska, USA is the main feature of this scene, with a transition from oceanic to land background (Figure 3). Extremely light and shallow rain and periodic overlying mid-level clouds with a freezing level near 1.5 km appear south of $60^\circ\text{N}/146.9^\circ\text{W}$ (Sector I, left-end side). A more intense and deeper (~ 5 km cloud top) rain core is located just north of $60^\circ\text{N}/146.9^\circ\text{W}$ (Sector I, right-end side), then the freezing level steadily declines. The surface rain/snow transition occurs near $61^\circ\text{N}/147.6^\circ\text{W}$, coincident with the ocean to land surface transition (Sector II). Here, coastal and orographic snow with embedded intense snowfall is located near $61.4^\circ\text{N}/147.9^\circ\text{W}$. The estimated surface 2C-SNOW snowfall rates approach $5 \text{ mm}\cdot\text{h}^{-1}$ in these embedded snow cores. SWC around $3 \times 10^{-4} \text{ kg}\cdot\text{m}^{-3}$ is located in the lowest portion of the coastal snow, while SWC exceeds $5 \times 10^{-4} \text{ kg}\cdot\text{m}^{-3}$ in the most intense snow core over mountainous terrain. Possible shallow and light surface snow exist over the mountains between $62.8^\circ\text{N}/149.0^\circ\text{W}$ and $64.2^\circ\text{N}/150.1^\circ\text{W}$ (Sector III). Elevated clouds not associated with surface snow above this mountainous shallow snow event are found to north and west through $\sim 65.0^\circ\text{N}/150.0^\circ\text{W}$ (Sector IV). Reflectivities are generally low, although cloud structure thickness is ~ 4 – 5 km, with cloud base (top) near 3–4 (8–9) km. Another shallow, mostly light, snowfall layer over land is also located in the far northwest portion of this scene (Sector V). The most intense reflectivities are generally under 10 dBZ located near $66.9^\circ\text{N}/152.7^\circ\text{W}$, and SWC and surface snowfall rates are accordingly low.

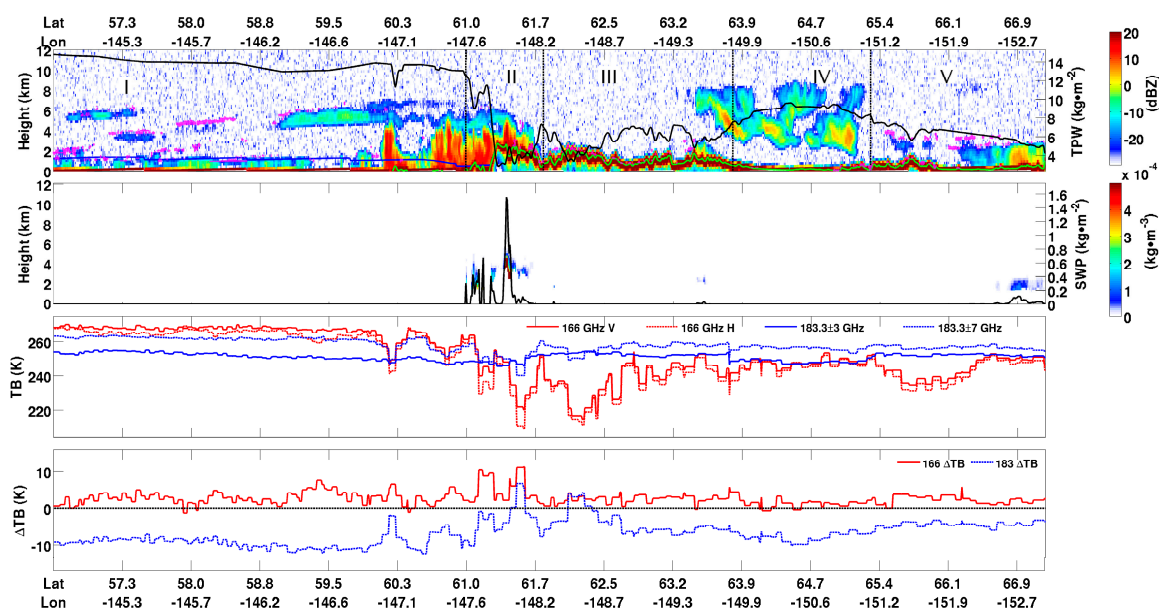


Figure 3. Same as in Figure 2a but for orographic event on 14 December 2014.

TPW values vary widely over this scene. The TPW is relative stable over the ocean (~ 11 – $12 \text{ kg}\cdot\text{m}^{-2}$), decreases sharply over the mountainous terrain (~ 4 – $7 \text{ kg}\cdot\text{m}^{-2}$), increases again to near $9 \text{ kg}\cdot\text{m}^{-2}$ over lower land surfaces near $64.2^\circ\text{N}/150.1^\circ\text{W}$, then steadily decreases to near $5 \text{ kg}\cdot\text{m}^{-2}$ in the far north and west portions of the scene. Unlike the first case study that showed a drastic TPW change corresponding to tangible 183.3 ± 3 TB changes, the 183.3 ± 3 GHz TBs associated with this case exhibit relatively subtle changes despite the varying TPW, with warmer TBs over ocean than over the mountain and land surfaces. The 183 ΔTB quickly transitions to a positive value

immediately to the north and west of the most intense precipitation over the highest terrain in the center of the scene ($\sim 60.7^\circ\text{N}/147.6^\circ\text{W}$), where TPW values are extremely low.

The 166 GHz and 183.3 ± 7 GHz channels also exhibit interesting and varying sensitivity to the precipitation structures in this scene. Over the ocean (Sector I), 166 GHz TBs are quite warm (~ 270 K) with 166 ΔTB values between 0 and 5 K. The shallow rainfall laden with cloud and rain liquid droplets greatly increases atmospheric opacity and virtually eliminates 166 GHz polarization differences that would be expected over the highly polarized ocean surface under clear skies. The 183.3 ± 7 GHz channel is insensitive to these shallow rain structures due to sufficient lower atmospheric opacity attributed to water vapor.

Two deeper rain structures located further to the north and west (Sector I, right-end side) again illustrate the sensitivity of high-frequency, scattering sensitive GMI channels to columnar ice. The deepest rain cloud near $59.4^\circ\text{N}/146.6^\circ\text{W}$ induces a ~ 30 (20) K 166 (183.3 ± 7) GHz TB reduction due to scattering by ice particles above the freezing level. The 166 ΔTB values also slightly increase due to this precipitation feature. The 183 ΔTB values, however, respond vigorously. The 183 ΔTB is an extremely valuable metric for some precipitation events due to the lack of 183.3 ± 3 GHz sensitivity to columnar ice in systems that are deep enough to affect 183.3 ± 7 GHz TBs, but with cloud tops low enough to allow sufficient water vapor absorption/emission to effectively render 183.3 ± 3 GHz measurements invariable. The second deep rain core near $60^\circ\text{N}/146.9^\circ\text{W}$ reaches as high, or slightly higher, than the previous rain feature, but reflectivity magnitudes are slightly lower. Both 166 GHz and 183.3 ± 7 GHz TB depressions are accordingly not as low—about 15–20 K for both channels. A 183 ΔTB signature also accompanies this feature, albeit with a smaller magnitude than the other rain feature.

The coastal and orographic snowfall (Sector II) shows interesting, yet different, 166 GHz responses compared to the deeper oceanic rain profiles. TBs at 166 and 183.3 ± 7 GHz both decrease in the deeper and most intense snowing cloud structures due to snow/ice scattering effects. The 166 GHz TBs show enhanced sensitivity and a much larger TB decrease (~ 20 – 30 K) compared to the 183.3 ± 7 GHz TBs near the intense upslope snowfall located near $60.4^\circ\text{N}/147.2^\circ\text{W}$. The intense upslope snow also corresponds to a noticeable polarized signal, with 166 ΔTB values near 10 K despite being located over an unpolarized land surface. This 166 GHz polarized signal is presumably also due to ice scattering effects [25]. Note that 166 GHz TB reductions are not as strong, however, just to the northwest in the snowfall core located at the highest elevations near $60.7^\circ\text{N}/147.6^\circ\text{W}$ despite SWP retrievals indicating the highest ice content in this region. Maximum SWP estimates exceed $1.5 \text{ kg}\cdot\text{m}^{-2}$ in this zone, compared to under $0.6 \text{ kg}\cdot\text{m}^{-2}$ in the most intense upslope snow located to the south and east. Surface emission at the highest elevations under low TPW conditions strongly affects the 166 GHz signal, much more than the 183.3 ± 7 GHz signal.

Moving further to the north and west, the 166 GHz channel displays a warming response to the very shallow snowfall event over higher terrain near $62.8^\circ\text{N}/149.0^\circ\text{W}$ (Sector III, right-end side). The 183 GHz TBs are unaffected by this shallow precipitation feature. The non-precipitating mid-level clouds further to north and west (Sector IV) show some 166 GHz TB reductions due to either ice scattering and/or surface emissivity effects, embedded in the significantly higher mean TB values (20 K) with respect to the adjacent clear sky regions (probably due to the higher TPW found in correspondence of these mid-level clouds, as confirmed by the very low 166 ΔTB ($\Delta\text{TB}\sim 0$ K)). It is worth noticing that there is an interesting sudden and concurrent decrease in 166 (~ 10 K) and both 183 GHz channel TBs (~ 5 K) near $63.0^\circ\text{N}/149.2^\circ\text{W}$ that corresponds to an increasing TPW zone and the elevated CPR reflectivities located at ~ 6 km altitude. This feature is probably related to scattering at all frequencies since sufficient ice content is located at high altitudes with low enough ambient water vapor values to cause a 183.3 ± 3 GHz weighting function downward shift that makes it sensitive to ice. Note that the 183 ΔTB values are stable in this zone, thus illustrating unison in the respective 183 GHz channel responses.

The final noteworthy precipitation feature is the shallow snow-producing cloud structure near $66^\circ\text{N}/152^\circ\text{W}$ (Sector V). The 166 GHz TBs increase of about 25 K in correspondence with these shallow

clouds compared to the clear sky region located near 65.5°N/151.3°W. This response is again due to the supercooled water emission as confirmed by the CloudSat DARDAR product (shown as magenta color cloud layers in the top panel) and is confirmed by the absence of a polarization signal related to this shallow cloud, as opposed to a slight polarization observed with the snow-covered background under clear skies. This again confirms previous studies [19,20] showing TB and Δ TB enhancement at 150 GHz in presence of snowfall, while damping of the polarization signal was observed in the presence of supercooled water. This also confirms the finding by Liu and Seo [44] that describes an emission signal at high frequencies in the winter associated with snowfall in the presence of a frozen surface background (low moisture and cold conditions). This effect was not visible at 166 GHz for the 30 April 2014 case study previously described because of the high TPW.

3.1.3. Case 3: Synoptic Snowfall Event over the Labrador Sea 27 March 2014

Figure 4a shows an extensive, deep synoptic snowfall case over the Labrador Sea between Greenland and the Canadian maritime provinces, with an open water/sea-ice transition around 61°N–58°W. This snowfall event occurred in a cold, dry environment (TPW < 10 kg·m⁻²) over the whole region, becoming extremely dry (TPW < 5 kg·m⁻²) over the sea ice formations (north of 60.5°N). CPR shows a 6–8 km deep cloud with peaks of reflectivity around 10–15 dBZ, associated with a SWP reaching 1.6 kg·m⁻² in correspondence of the deepest cloud (Sector I). Peak SWP values are associated with particularly high SWC located above 6 km southward of 57.5°N. Shallow snowfall structures also appear as a distinctive separate cloud structure northward of about 59.8°N–57.2°W, although embedded shallow convective structures are also evident in the lowest ~1 km as far south as about 58.4°N (Sector II).

The 166 Δ TB is around 10–15 K in the most intense portion of the cloud over ocean. It increases gradually as the cloud gets less intense, and as TPW decreases, because of the increasing surface emission contribution to the signal, exceeding 20 K between 59.6°N and 61°N (Sector III). Here, CPR evidences the presence of a multilayer cloud, with a shallow cloud layer (<1 km thick), and a higher level cloud with maximum reflectivity around 0 dBZ. The spotty snowfall retrieval in this sector, particularly evident around 60°N, is due to the weak reflectivity signal at the lower bins, and to the fact that 2C-SNOW product provides SWC profile only if Z at the first clutter free bin is higher than -15 dBZ. The increase of Δ TB in this region is due to a combination of effects: the effect of the sea surface, the possible existence of mixed-phase clouds containing supercooled water, and the polarization effect induced by the ice crystals in the upper level cloud. In fact, 166 Δ TB starts decreasing north of 61°N (Sector IV), where an upper level cloud exists that is not associated with precipitation, but sea ice is present at the surface (as evidenced by the GMI TB maps at frequencies below 89 GHz in Figure 4b, and confirmed by the sea ice concentration map (not shown)). This shows that the upper level cloud alone does not explain the high 166 Δ TB observed over the open water region, which is mostly due to the surface. In the cloud free regions, the mean Δ TB value in presence of sea ice is below 10 K (lower than the values over ocean in presence of intense snowfall as evidenced also in Figure 4b), and both TBs and 166 Δ TB show a large variability. It is worth noting the large range of variability of TBs at 166 GHz (both V-pol and H-pol) for this event compared to the 183.3 GHz channels, with values ranging between 205 K (for the deepest cloud) and 220 K (for the multilayer cloud) for 166 GHz H-pol and between 220 K (for the deepest cloud) and 245 K (for the multilayer cloud) for 166 GHz V-pol, with TB for H-pol always lower than V-pol as evidenced also by Gong and Wu [25]. The 183 Δ TB shows positive values up to about 10 K in correspondence of the deeper and most intense snowfall (Sector I, see also bottom right panel in Figure 4b) and negative values elsewhere. However, it shows values and variability similar to the clear sky region over sea ice (Sector IV), where all TBs below 37 GHz show large variability related to sea-ice concentration.

This case study shows that the proper characterization of the state of the sea surface at higher latitudes, especially in dry conditions (TPW < 10 kg·m⁻²), is necessary to be able to correctly interpret the GMI signal at high frequencies and relate it to snowfall: on one side, low frequency channels can

be effectively used to delineate regions of sea ice and different sea-ice concentration, as shown in the top panels of Figure 4b, with large variability over the sea ice and no signal related to the cloud even in correspondence of the snowfall region; on the other side the use of the high-frequency channels, and in particular the use of 166 and 183 Δ TBs, can provided the information needed to correctly interpret the signal related to snowfall (see bottom panels in Figure 4b).

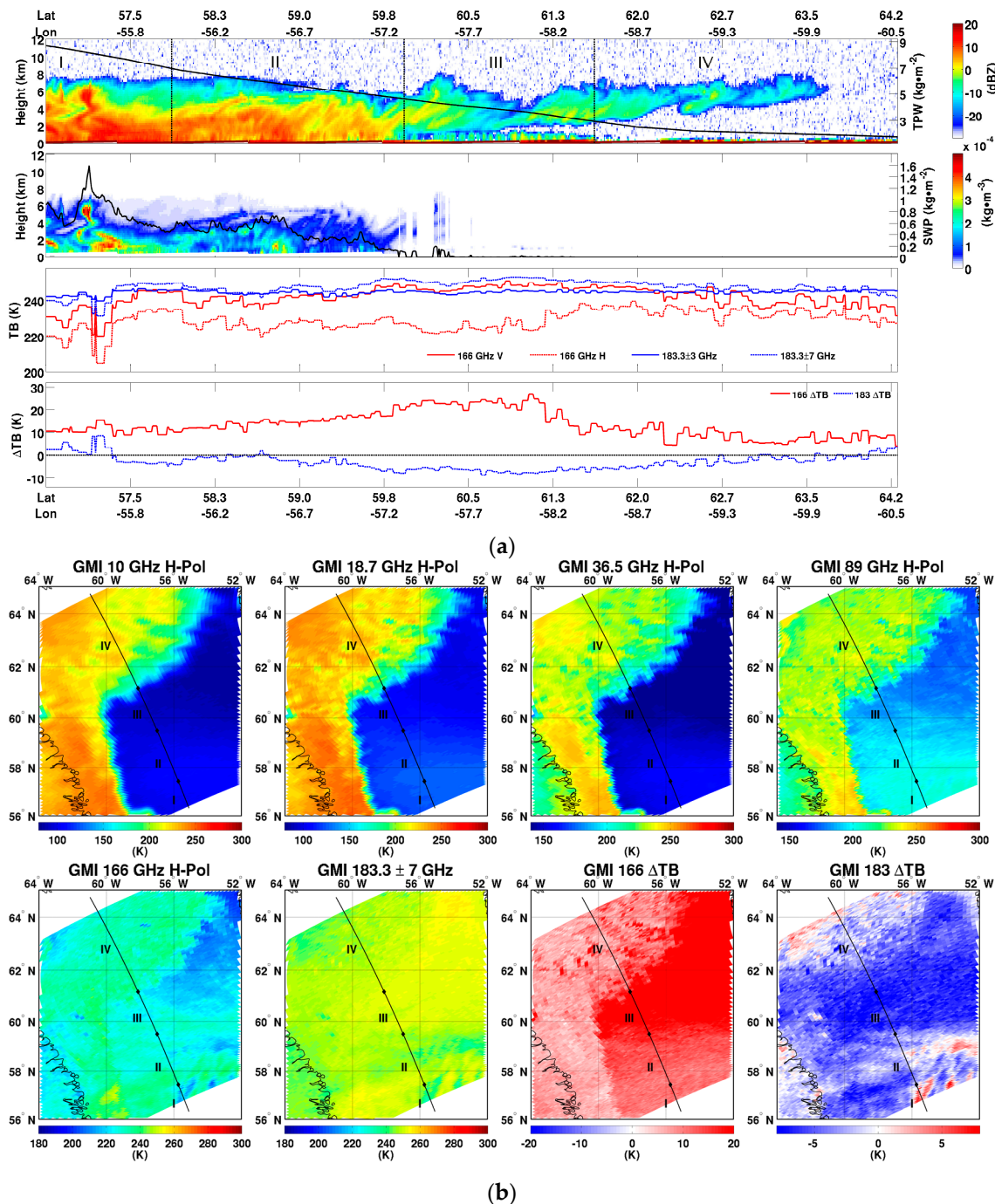


Figure 4. Synoptic snowfall event over the Labrador Sea on 27 March 2014. (a) Same as in Figure 2a; (b) Same as in Figure 2b.

The three case studies illustrate the complicated and multi-faceted TB signatures associated with different snowfall modes (e.g., deep versus shallow snow layers) and cloud microphysical composition

under different ambient atmospheric conditions over varying surfaces. They also illustrate the value of high-frequency GMI channels to elicit new ways of exploring such events.

3.2. Analysis of the 166 GHz Channel Capabilities for Snowfall Detection

To define some general, more quantitative criteria on the use of GMI 166 GHz channels, and in particular the polarization signal at 166 GHz (166 Δ TB), for snowfall detection, a global GMI-CPR dataset analysis is carried out in this section. It is worth noting that GMI is the first spaceborne radiometer equipped with high frequency (>100 GHz) dual-polarization channels and, while numerous previous studies have thoroughly studied 183 GHz channels for surface snowfall applications [6,21–23], few studies have analyzed high frequency channel polarization sensitivity to snowfall [19,20], and these are based on ground-based measurements.

In this analysis, all the variables associated with CPR profiles (e.g., SWC, SWP, surface snowfall rate, TPW) are averaged to obtain a one-to-one correspondence between GMI TBs and CPR variables and without altering GMI observations, therefore the values shown in this section are different from those shown in the case studies analysis, where they were at the native CPR spatial resolution. The analysis is carried out considering as snow events the pixels where the averaged CPR 2C-SNOW surface snowfall rate is higher than 0 mm·h⁻¹.

3.2.1. Regression Tree Analysis of 166 GHz Δ TB

To extract meaningful information from GMI-CPR coincident dataset, we sought to clusterize our dataset using the environmental variables and cloud properties qualitatively outlined in Section 3.1 that influence the GMI TBs. In this study, the 166 Δ TB (named thereafter the target variable) has been analyzed. The clusterization has been conducted using a decision tree (regression tree) analysis [45,46]. This method hierarchically splits the observations into sub-groups using environmental parameters and cloud properties as input variables to minimize the variance within a sub-group. The observation partitioning ends when no significant improvement in the variance reduction can be obtained by the tree model (see Therneau and Atkinson [46] for details). Thus, the regression tree analysis finds different regimes (or sub-groups, identified through the input variables) explaining the variability of the target variable, without making any a priori assumption. In our study, the decision tree allowed identifying statistically different regimes in terms of environmental variables or cloud properties. Then, the snow detection and quantification potential of any of these sub-groups has been evaluated. To ensure that the sub-groups are statistically significant, only those containing at least 10% of the total number of observations in the dataset have been maintained. The input variables used in this analysis are: (1) the surface type (land, sea, coast flag (where coast is identified by any mix of land and sea) and sea ice concentration; (2) T_{2m} and TPW; (3) DARDAR product integrated ice water content (IWP), ice cloud top and bottom of ice altitude, altitude of maximum of ice content, ice cloud thickness, mean effective radius of ice, altitude of largest effective radius, flag for presence of supercooled water (embedded and on top of cloud layer), altitude of supercooled water layer; (4) 2C-SNOW product SWP, snow layer top and bottom height, altitude of maximum SWC, thickness of the snow layer; and (5) 2B-CLDCLASS cloud classification.

The 166 Δ TB tree analysis is shown in Figure 5. The input variables selected hierarchically by the tree algorithm and defining the sub-groups are represented in each node, from the most relevant to the least relevant (in terms of their impact on 166 Δ TB variability) going from the top to the bottom. Each branch represents a sub-group, defined by the condition indicated for each input variable found by the tree (e.g., for the first node (Surface type), the tree identifies the two subgroups, land surface, represented on the left part of the tree, and ocean/coast on the right part of the tree). For the final sub-groups (or final “leaves”), two quantities are computed to analyze if the conditions identified by the tree are favorable to snowfall detection and quantification: the mean 166 Δ TB value ($\langle \Delta$ TB \rangle), and the correlation coefficient (r) between 166 Δ TB and the snowfall amount, or SWP (when 2C-SNOW SWP > 0.0 kg·m⁻²).

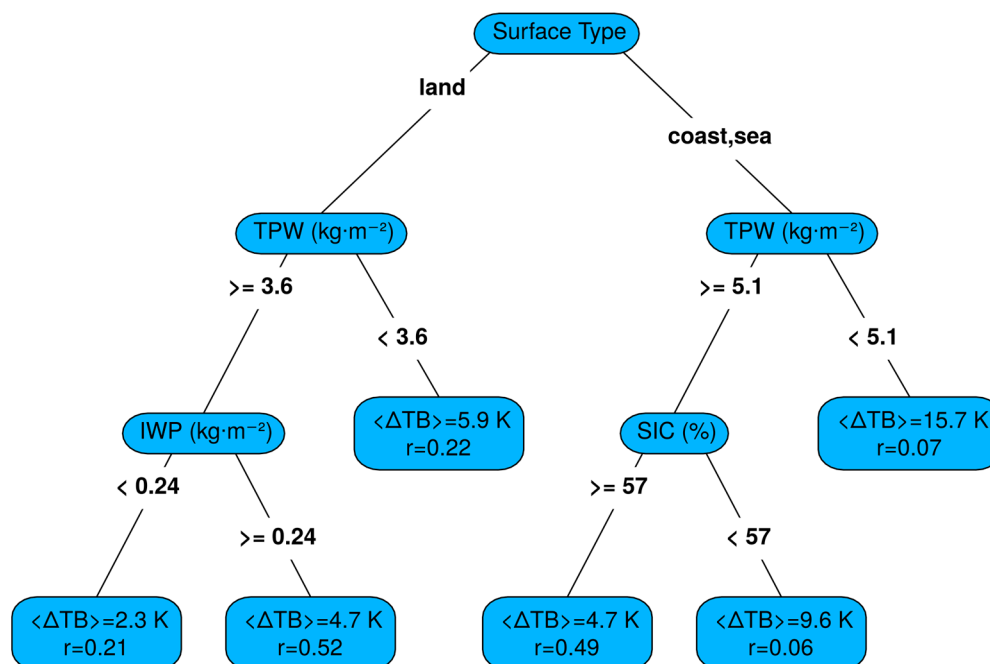


Figure 5. Regression tree results for 166 ΔTB (target variable) using the GMI-CPR coincident dataset environmental variables and cloud properties as input variables. Each node (blue ovals) shows the relevant variable found by the tree (hierarchically from the top to the bottom). Each branch (or sub-group) is identified by the thresholds of the variable in the corresponding node and indicated on the black lines. For the final sub-groups, or final “leaves” (blue rectangles), the mean 166 ΔTB value ($\langle \Delta TB \rangle$), and the correlation coefficient (r) between 166 ΔTB and SWP are provided. Only sub-groups containing at least 10% of the total number of observations are considered (see text for details).

The first node shows that the tree selects the surface type (land and ocean/coast) as the first variable explaining 166 ΔTB variability. In the two lower branches (land (left side) and sea/coast (right side)) among all the input variables, TPW is the most important variable selected by the tree. Over land in very dry conditions ($TPW < 3.6 \text{ kg}\cdot\text{m}^{-2}$, right branch), the mean ΔTB equals 5.9 K and it has low correlation with the intensity of snowfall ($r = 0.22$). In moister conditions ($TPW \geq 3.6 \text{ kg}\cdot\text{m}^{-2}$), the DARDAR IWP is found by the tree as the third relevant variable impacting 166 ΔTB behavior. It is worth noting that 88% of snowfall land pixels in the GMI-CPR dataset are found at $T_{2m} < 270 \text{ K}$, and, therefore, likely snow covered, and that the IWP is highly correlated to the snowfall amount (i.e., the 2C-SNOW SWP) (correlation coefficient larger than 0.9). For larger snowfall amounts (associated with $IWP \geq 0.24 \text{ kg}\cdot\text{m}^{-2}$), mean 166 ΔTB values and the correlation are higher ($\langle \Delta TB \rangle = 4.7 \text{ K}$, $r = 0.52$), while for lower snowfall amounts (associated with $IWP < 0.24 \text{ kg}\cdot\text{m}^{-2}$), both mean ΔTB values and correlation are lower ($\langle \Delta TB \rangle = 2.3 \text{ K}$, $r = 0.21$). These results show that over land 166 ΔTB can be a useful parameter to identify snowfall mainly in moist conditions and for moderate to heavy snowfall amounts. In such conditions, its variability is somewhat correlated to the snowfall amount. In very dry conditions, or in the presence of weak snowfall, 166 ΔTB variability is not significantly correlated to the snowfall amount, therefore it is not useful for snowfall detection.

Over sea (and coast), the TPW threshold is higher than over land ($TPW \geq 5.1 \text{ kg}\cdot\text{m}^{-2}$), due to the stronger impact of the surface on the 166 GHz polarization: higher water vapor amounts are needed to partly mask the background surface effect on the 166 ΔTB signal. In dry conditions ($TPW < 5.1 \text{ kg}\cdot\text{m}^{-2}$, right branch), the 166 ΔTB values are very high ($\langle \Delta TB \rangle = 15.7 \text{ K}$, due to the impact of the surface) and the correlation of ΔTB with snowfall is close to 0 ($r = 0.07$) independently of other parameters. In moister conditions ($TPW \geq 5.1 \text{ kg}\cdot\text{m}^{-2}$), the sea ice concentration (SIC) appears as the main variable to explain the 166 ΔTB variability. For $SIC < 57\%$, ΔTB still shows high values ($\langle \Delta TB \rangle = 9.6 \text{ K}$), and the

correlation with snowfall is again close to 0. However, for $SIC \geq 57\%$ the correlation with snowfall increases significantly ($r = 0.49$) regardless of the snowfall amount. In summary, over sea ice and in moister conditions ($TPW > 5.1 \text{ kg}\cdot\text{m}^{-2}$) over land, 166 ΔTB can be a valuable source of information for snowfall detection and quantification, while over open water (or for low sea ice concentrations) the surface impact on 166 ΔTB masks any signal related to the snowfall and the TBs (or TB differences at 183.3 GHz) need to be exploited.

3.2.2. Analysis of 166 GHz ΔTB and TB Sensitivity to CPR Snowfall

To investigate further the 166 ΔTB sensitivity to snowfall, we analyze the relationship between ΔTB and TBs at 166 GHz in relation to the significant environmental conditions highlighted in the previous section (surface type, and TPW), and snowfall amount (SWP). It is worth noting that, as opposed to Gong and Wu [25], the analysis focuses mostly on higher latitudes (around 60°N/S) because it is carried out only for snowfall pixels in the GMI-CPR coincident datasets (see Figure 1). The 2C-SNOW SWP was used to identify snowfall profiles. Such identification is subject to the limitation of the 2C-SNOW product evidenced in Section 2. On the one hand, the snowfall manifold, made of profiles where $SWP > 0 \text{ kg}\cdot\text{m}^{-2}$ (i.e., containing snow at the surface according to 2C-SNOW product), may have SWP underestimated (i.e., because snowfall below the first clutter-free bin level is missed in the 2C-SNOW product). On the other hand, it might exclude snowfall profiles with a weak signal (Z at the first clutter-free bin level below -15 dBZ), or shallow snowfall events, for which $2C\text{-SNOW } SWP = 0 \text{ kg}\cdot\text{m}^{-2}$.

Figure 6 shows the distribution and occurrences (2-D histogram) of the snowfall pixels of the whole GMI-CPR dataset in the 166 GHz ΔTB -TB 2-D space (divided into 200×100 bins). Each dot represents the mean ΔTB and TB values in each bin while the color bar indicates the percentage of occurrences. Contours identifying the 90% of occurrences in the snowfall manifolds associated with the different background surfaces identified by the tree analysis (land, open water, sea ice) are also shown. The SIC concentration found by the regression tree analysis ($SIC > 57\%$) has been used to separate sea ice from open water. While 166 ΔTB s are positive, as in Gong and Wu [25], the distinctive bell-shaped ΔTB curve as a function of V-pol TB (peaking near 10 K) is not found. The minimum TBs are rarely found below 200 K because of the weak scattering effect by the ice particles associated with snowfall at higher latitudes. Moreover, the behavior of 166 ΔTB versus TB in the upper right portion of the scatterplot (for the whole and open water manifolds) corresponds to what is shown in Gong and Wu [25] at 89 GHz. The highly polarized signal (high 166 ΔTB values) is due to the large impact of the background surface and to the low opacity of the atmosphere in dry conditions. There is a very distinct behavior of the ΔTB -TB relation for the three different surface types. It is worth noting the different shape and range of 166 ΔTB values of the sea ice manifold with respect to the open water manifold, and its similarity to the land manifold due to the lower polarization found in both cases with respect to open water. The range of TB values at 166 GHz (V-pol, but the same holds for H-pol) for the three manifolds, however, is quite different.

Figure 7 shows the same distribution of the snowfall pixels as Figure 6 in the ΔTB -TB 2-D space with mean SWP and TPW values for each bin indicated by the color bars. The results are shown for land (with $T_{2m} < 270 \text{ K}$ for 88% of pixels), open water ($SIC < 57\%$), and sea ice ($SIC > 57\%$). Over land we observe that for $TPW > 3\text{--}4 \text{ kg}\cdot\text{m}^{-2}$, for any given TB value, ΔTB increases as the SWP increases, showing a good correlation between 166 ΔTB and snowfall. These results reflect what was found in the regression tree analysis, confirming that ΔTB can be a valuable parameter for snowfall detection over land when the atmosphere is moist enough to mask the signal from the radiatively cold background (i.e., $TPW > 3.5 \text{ kg}\cdot\text{m}^{-2}$). For lower values of TPW, there is no evidence of a relationship between ΔTB or TB with the SWP. The same holds for 166 GHz TB (V-pol) $> 260 \text{ K}$. In this region of the scatter diagram where the bins are characterized by large TPW ($TPW > 10 \text{ kg}\cdot\text{m}^{-2}$) and low SWP values ($SWP < 0.01 \text{ kg}\cdot\text{m}^{-2}$), the water vapor dampens the polarization effect at 166 GHz, while its emission

reduces the weak scattering effect due to the snow. It is also worth noticing that the largest snowfall amounts ($SWP > 0.5 \text{ kg}\cdot\text{m}^{-2}$) are mostly found for $220 \text{ K} < TB < 260 \text{ K}$.

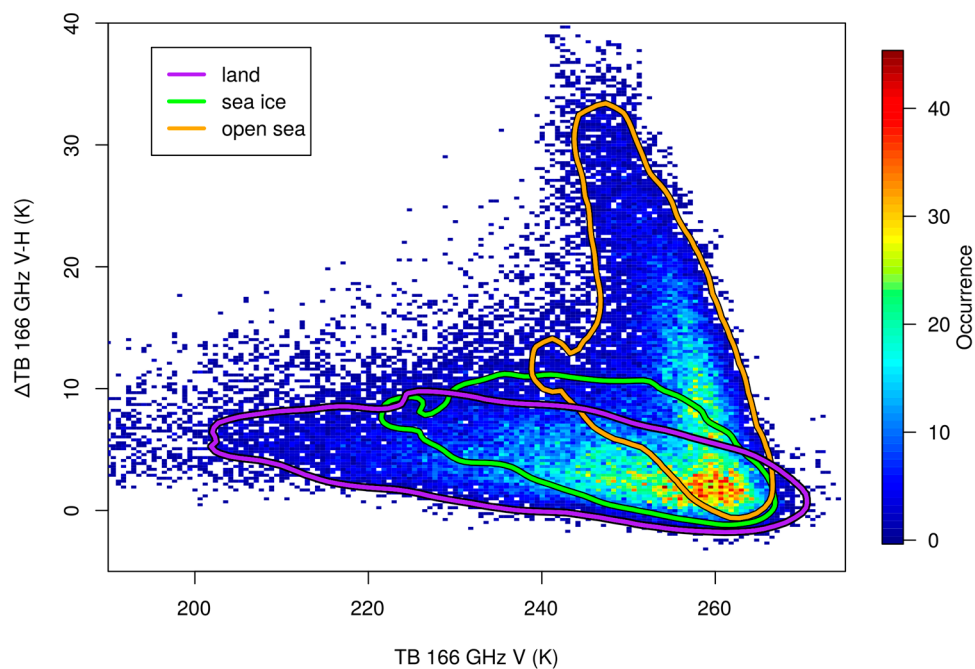


Figure 6. Scatterplot of the 166 GHz ΔTB -TB 2-D histograms for the whole GMI-CPR snowfall dataset. The 2-D histogram is created by dividing the ΔTB -TB space in 200×100 bins. Each dot represents the mean ΔTB or TB value in each 2-D bin while the color bar indicates the percentage of occurrences. Contours for 90% occurrences in the three background surface manifolds are also superimposed: open water (orange), land (purple), sea ice (SIC > 57%) (green).

Over ocean (open water or SIC < 57%) two different regions can be identified. Depending on the snowfall regime the behavior of ΔTB versus TB changes significantly. One region is characterized by a linear relationship between ΔTB and TB for the lower SWP values ($SWP < 0.1 \text{ kg}\cdot\text{m}^{-2}$), with decreasing ΔTB (from 30 K to 0 K), and increasing TB (from 260 K to 270 K) as TPW increases, as expected, and with a slight dependence on SWP. In this region, the ΔTB signal is either dominated by the surface contribution or by the dampening effect on the TB polarization by the water vapor. The other region is characterized by the largest values of SWP ($SWP > 0.1 \text{ kg}\cdot\text{m}^{-2}$) associated with high values of TPW, but also in this case the impact of snowfall on the TB polarization is not significant. As also evidenced in the regression tree analysis, over open water ΔTB is not related to snowfall due to the high polarization induced by the surface. On the other hand, 166 GHz TBs are more correlated with SWP, as the lowest TBs are associated with the highest SWP. Therefore, over open water (or low SIC), TBs at 166 GHz could be used to retrieve snowfall intensity, mostly in presence of intense snowfall events and moist conditions ($SWP > 0.5 \text{ kg}\cdot\text{m}^{-2}$, and $TPW > 10 \text{ kg}\cdot\text{m}^{-2}$ as evidenced in Figure 7).

Over sea ice, the almost linear relationship found between ΔTB and TB is similar to the land signature because of the lower impact on the polarization due to the water surface. The ΔTB signal is also strongly related to the SWP (decreasing as the SWP increases). TPW has a lower range of values with respect to open water, with TPW mostly $< 5 \text{ kg}\cdot\text{m}^{-2}$. These results again confirm what was found in the regression tree analysis, showing that 166 ΔTB can be a useful variable for snowfall detection (and retrieval) over sea ice, as well as over land. As SWP increases, 166 ΔTB increases when the TPW is above a given threshold (lower over land than over sea ice) according to the regression tree analysis and as confirmed by the results shown in Figure 7. However, while over land TPW has a much larger range of variability and TBs at 166 GHz (ranging from 170 K to 270 K) do not show

a strong relationship with SWP, over sea ice TPW variability is lower, and the TBs show a stronger dependence on SWP, decreasing from 270 K to around 220 K as SWP increases.

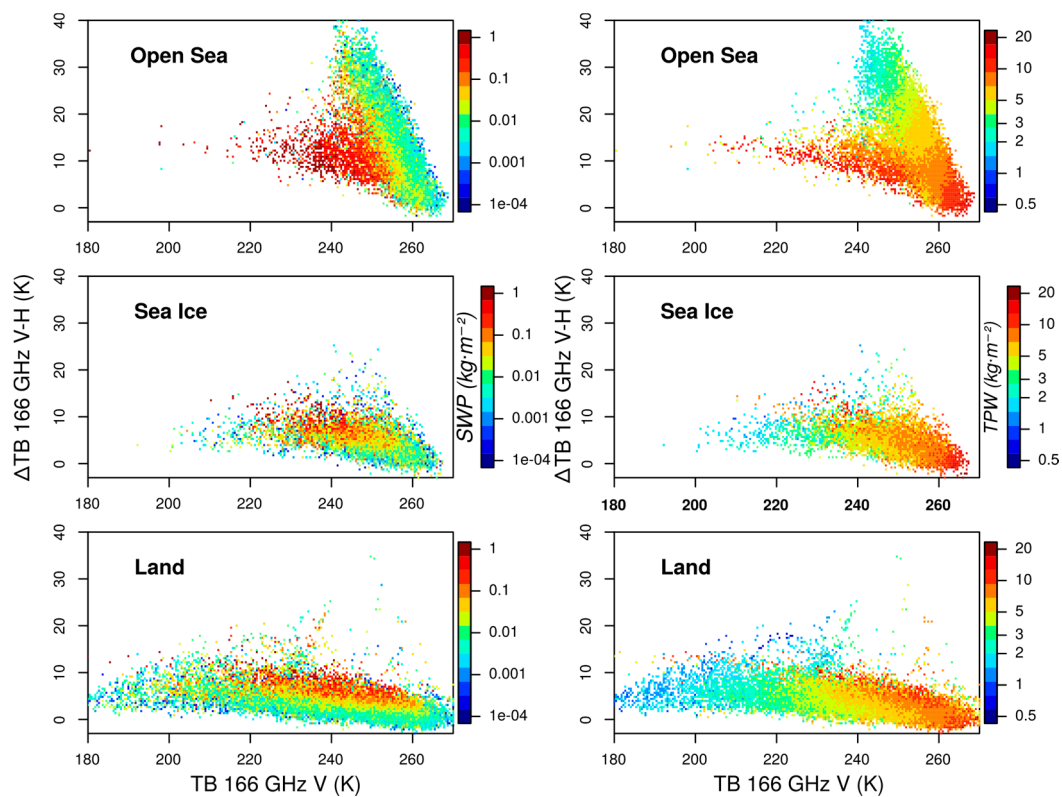


Figure 7. Scatterplots of the Δ TB-TB for snowfall pixels in the three surface type manifolds: open sea (SIC < 57%) (top); sea ice (SIC > 57%) (middle); and land (bottom). Δ TB-TB space is divided into 200×100 bins, and the mean SWP (left); and TPW (right) values in each Δ TB and TB bin are represented (in log scale).

3.2.3. Impact of Supercooled Droplets on 166 GHz TB and Δ TB

In Section 3.1 we highlighted the significant impact that a supercooled water layer can have on TBs and Δ TB at 166 GHz. We have also evidenced that such an impact is strongly dependent on the environmental conditions. Although we included this variable in the regression tree, this variable was not selected by the algorithm to explain the variability of Δ TB. Likely, the effect of supercooled water on 166 Δ TB is masked by other predominant factors such as surface type or humidity. To analyze further the sensitivity of the GMI 166 GHz channels to snowfall, and to illustrate the impact of supercooled droplets on the signal, we have compared the behavior of both Δ TB and TB in clear sky to that in presence of snowfall, and in presence of snowfall and supercooled droplets (embedded in the cloud, or at the top layers of the cloud, which occurred in 72% of snowfall cases) as inferred from the CloudSat DARDAR product. The whole GMI-CPR dataset has been divided into four sub-groups: clear sky (CS, which means $SWP = 0 \text{ kg}\cdot\text{m}^{-2}$), snowfall (SN, for $SWP > 0 \text{ kg}\cdot\text{m}^{-2}$, and no supercooled water), snow with supercooled droplets on the top cloud layers (SCT), and snow with supercooled droplets embedded in the cloud (SCE). It is worth noting that the radar-lidar combination in the DARDAR product is very useful for distinguishing cloud phase (e.g., Ceccaldi et al. [47]). While the lidar can identify accurately the presence of a supercooled layer on top of the cloud, the embedded supercooled droplets identification is less certain as it might be missed in some cases (J. Delanoë, personal communication). Therefore, the snowfall manifold (SN) might include cloud profiles with supercooled droplets embedded in the cloud. Moreover, the clear-sky (CS) manifold might include shallow or weak snowfall cases (with or without supercooled droplets) missed by the 2C-SNOW

product (as evidenced in the case study analysis in Section 3.1). However, we have verified that it is meaningful to analyze the sensitivity of the GMI 166 GHz channels to snowfall considering these different manifolds (SN, SCT, SCE, and CS) by testing that the distributions of 166 Δ TB and TB for each pair of manifolds are statistically different from each other. Each sub-group has been categorized in bins according to TPW (dividing the TPW range in 21 bins) and according to SWP (dividing the SWP range in 11 bins). Then, for each subgroup and for each bin, the median 166 Δ TB and TB values have been computed. Figures 8 and 9 show the median values found in each bin (TB V-pol in Figure 8, and Δ TB in Figure 9), as a function of the TPW (top panels) and SWP (bottom panels). The results are shown for land and sea ice, the conditions where 166 Δ TB responds mostly to the cloud and is less contaminated by the surface. The thresholds for TPW ($3.6 \text{ kg}\cdot\text{m}^{-2}$) and sea ice concentration (SIC > 57%) found in the regression tree analysis, and confirmed in the analysis of Figure 7, are used in Figures 8 and 9 to better capture the relation with SWP, and isolate the impact of supercooled droplets on the signal.

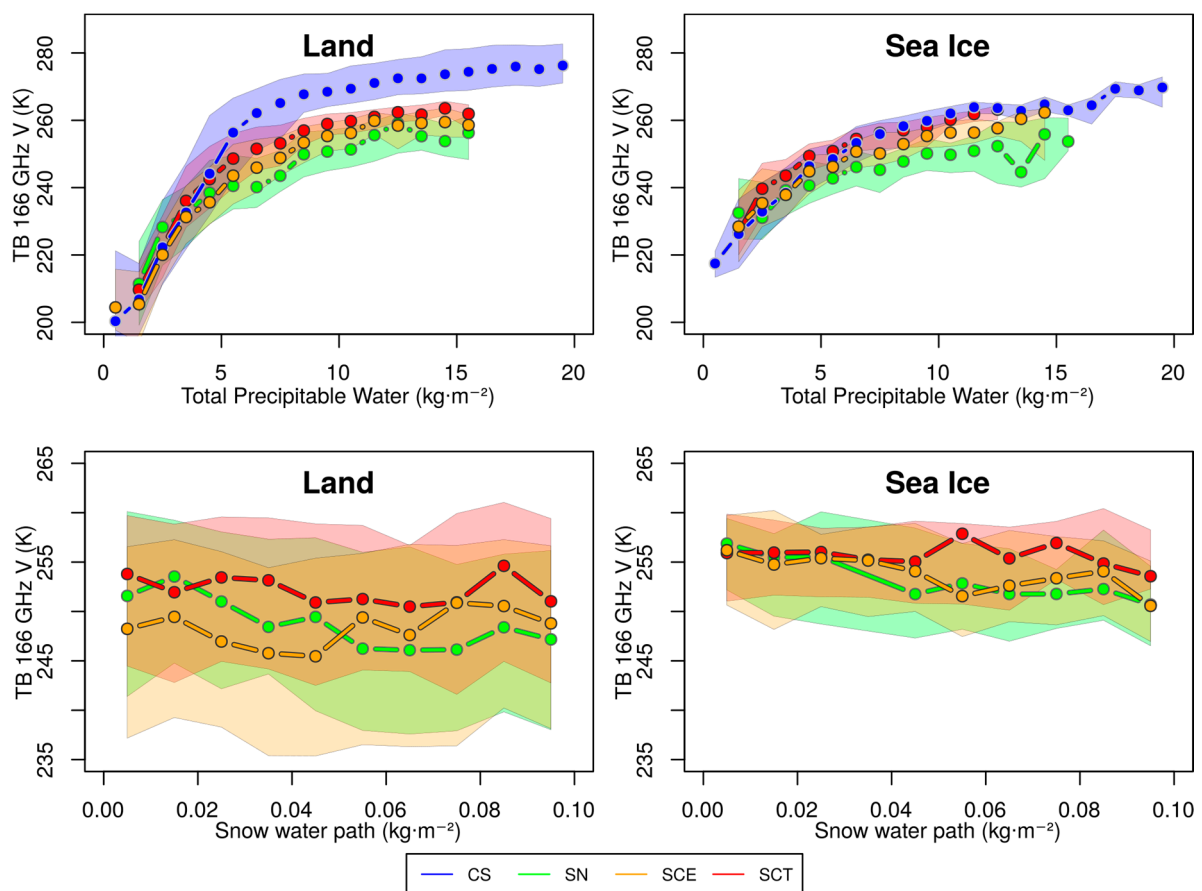


Figure 8. Median values of TBs at 166 GHz (V-pol) (computed in TPW and SWP bins) as functions of: TPW (**top**); and SWP (**bottom**) for clear sky (CS, blue), snow (SN, green), snow + embedded layer of supercooled (SCE, orange), snow+ supercooled layer on top (SCT, red). The colored shades represent the spread of the TBs between the 25th and 75th percentiles in each manifold. The dataset has been divided into 21 TPW bins (top) and 11 SWP bins (bottom), and only the results for bins with at least 20 pixels are shown (for statistical significance). Sea ice results are shown for SIC > 57%. In the bottom panels the results are shown for TPW > $3.6 \text{ kg}\cdot\text{m}^{-2}$ over land, and for TPW > $5.1 \text{ kg}\cdot\text{m}^{-2}$ over sea ice.

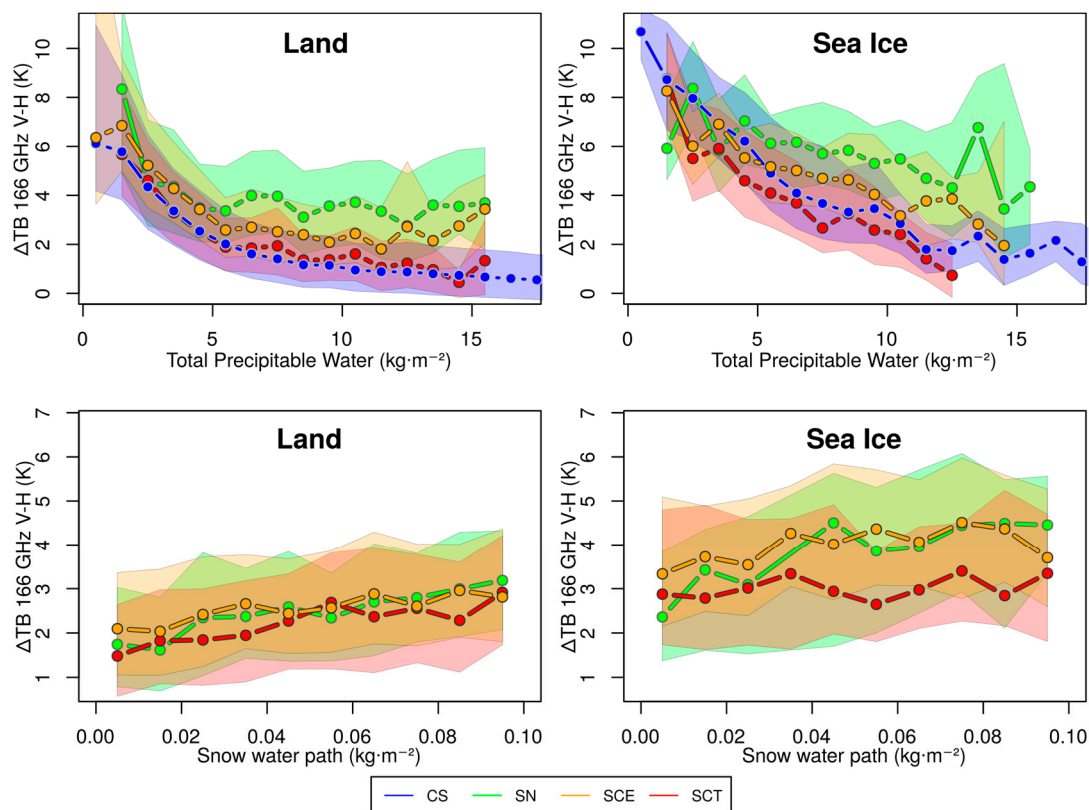


Figure 9. Same as in Figure 8 but for 166 GHz ΔTB .

In Figure 8, over land, median TBs increase with TPW (as expected because of the increasing emission by the water vapor), and in presence of snowfall, and for $TPW > 4 \text{ kg}\cdot\text{m}^{-2}$ (close to the TPW threshold found by the regression tree analysis), the median TBs of snowfall cases are systematically lower compared to clear sky (because of the scattering by the ice). However, the presence of supercooled droplets significantly impacts the TBs, especially when they are found on the top of ice cloud layers (SCT). In such cases, median TBs can be up to 10 K higher (on average) than snow-only cases. This is due to the emission by the water droplets and also to the fact that, on average for each TPW bin, the SWP found in presence of supercooled droplets is lower than for snowfall clouds with no supercooled droplets (on the whole dataset SWP mean values are $0.04 \text{ kg}\cdot\text{m}^{-2}$ for SCT, $0.10 \text{ kg}\cdot\text{m}^{-2}$ for SCE, and $0.21 \text{ kg}\cdot\text{m}^{-2}$ for SN). Looking at the median TB behavior as a function of SWP (Figure 8, bottom-left panel), it is evident that there is a decrease of TBs for SN (snowfall cases) as SWP increases and exceeds $0.03 \text{ kg}\cdot\text{m}^{-2}$. The effect of the supercooled droplets, however, is very significant, and it attenuates the ice scattering effect (shown for SN by the TBs decreasing as SWP increases), especially when droplets are found on the top of the ice cloud layer (SCT). When the supercooled droplets are embedded in the cloud (SCE) the effect is less clear, median TBs appear lower than snow-only cases for $SWP < 0.04\text{--}0.05 \text{ kg}\cdot\text{m}^{-2}$ and higher for larger SWP values. It is worth noting that in presence of supercooled droplets over land (both SCT and SCE), 166 GHz TBs do not show a significant trend with the SWP because the cloud droplet emission compensates for the scattering effects by the ice cloud.

Over sea ice ($SIC > 57\%$), a clear distinction of the median 166 GHz TBs versus TPW curves in clear sky (CS) and with snowfall (SN) is visible only for $TPW > 4 \text{ kg}\cdot\text{m}^{-2}$, with median TBs lower for SN than for CS (Figure 8, top-right panel). In such conditions, the effect of the supercooled droplets is to significantly increase the TBs up to values comparable to CS when they are on top of the ice cloud layer (SCT), and to values between CS and SN when they are embedded in the cloud (SCE). In very dry conditions ($TPW < 5 \text{ kg}\cdot\text{m}^{-2}$), the supercooled droplet emission effect on TBs is noticeable. When they are on top of the cloud layer (SCT), TBs are higher than for CS or for SN. When the

supercooled droplets are embedded in the cloud (SCE), the effect of the emission by the droplets is reduced, and median TBs become comparable to CS (or to SN). It is worth noting that over land (top left panel), in very dry conditions, all curves almost overlap to each other, showing no effect of the presence of supercooled droplets on the median TBs. However, the effects of supercooled droplets on the TBs were highlighted in the case study analysis (Section 3.1.2). In very cold and dry conditions (i.e., and when the emission by the water vapor at 166 GHz is negligible) (e.g., northern portion of the Frontal snowfall case (Section 3.1.1), and Orographic case (Section 3.1.2)) supercooled droplets on top of the ice cloud layer corresponded to 166 GHz TB increases in presence of snowfall with respect to the clear sky region. We also noticed that, in moister conditions, such effects are masked by the water vapor emission (southern portion of the Frontal snowfall system, Section 3.1.1). In both cases, the background surface was land (very likely snow covered).

The effect of supercooled droplets is also evident in the bottom-right panel (sea ice). Here we note a trend of the TBs with the SWP (TBs decrease as SWP increase) for $SWP < 0.04\text{--}0.05 \text{ kg}\cdot\text{m}^{-2}$, while for larger amounts of snowfall such a trend is not evident (analogously to what was found over land). In presence of supercooled droplets, median TBs are found comparable to snowfall-only cases (SN) when they are embedded in the cloud (SCE) and for any value of SWP. When they are on top of the ice cloud layer (SCT), and for $SWP > 0.04\text{--}0.05 \text{ kg}\cdot\text{m}^{-2}$, the effect is to reduce the scattering effect on the TBs, and the associated TBs are up to 8–10 K (on average) higher compared to SN. These results show that also over sea ice the use of TBs at 166 GHz for snowfall detection can be quite problematic in presence of supercooled water droplets.

Note that the significance of the results shown in Figure 8 (i.e., presence or absence of trends) has been tested by carrying out a statistical test on the Spearman correlation coefficient for each pair of variables (TB vs. SWP, and TB vs. TPW) in each manifold (for the ranges shown in Figure 8). The test confirmed that all trends shown over land and sea ice in Figure 8 by the median values are significant and represent the trends between the two variables in each manifold, except for SCE over land, and for SCT over land and sea ice (i.e., no trend was evidenced in these cases, as shown in Figure 8).

In Figure 9 the behavior of the median 166 ΔTB for the different sub-groups is analyzed. Over land (top-left panel), for $TPW < 4\text{--}5 \text{ kg}\cdot\text{m}^{-2}$ it is evident the polarization by the surface in clear sky. For $TPW > 4\text{--}5 \text{ kg}\cdot\text{m}^{-2}$, SN shows higher ΔTB values than CS due to the polarization effect by the ice at 166 GHz (see also Gong and Wu [25]). In presence of supercooled droplets such effects are reduced, as the emission effect decreases the ice polarization effect. ΔTB median values are correspondingly lower compared to SN, and become comparable to clear-sky conditions when the droplets are found on top of the ice cloud. As pointed out above, this is also because, for each TPW bin, SCT cases (and to a less extent SCE cases) are associated with SWP lower than for SN cases. It is very interesting to note that, as opposed to the TBs (Figure 8), ΔTB shows a very distinct trend in presence of snowfall, with ΔTB increasing as SWP increases (for $SWP > 0.02 \text{ kg}\cdot\text{m}^{-2}$) (median values increasing from 1.5 K to 3 K as SWP increases). It is worth noting that these median values (e.g., ranging from 1.62 K to 3.18 K for SN, from 2.04 K to 2.96 K for SCE, and from 1.48 K to 2.91 K for SCT over land) are much lower than what can be found for single snowfall events (e.g., ranging from -2.78 K to 28.83 K for SN, from -2.49 K to 15.49 K for SCE, from -3.28 K to 21.76 K for SCT over land). This was also evidenced in the case study analysis (Section 3.1), where, in the presence of snowfall, ΔTB could be as high as 10–15 K. In presence of supercooled droplets such trends are still visible (Figure 9, lower-left panel), and the behavior is similar when they are on top of the ice cloud or embedded in the cloud (SCT and SCE), as opposed to what is shown for 166 GHz TBs (Figure 8).

These results show that the depolarization effect at 166 GHz induced by the cloud droplets is on average not enough to eliminate completely the polarization effect at 166 GHz by the ice crystals in presence of snowfall. This shows that ΔTB can be a very valuable parameter to use for snowfall detection and quantification for the following difficult circumstances: (1) over land, (2) for very weak snowfall events (very low SWP), and (3) for low TPW values in $4\text{--}5 \text{ kg}\cdot\text{m}^{-2}$ range (consistently to what found in the regression tree analysis). Over sea ice (SIC > 57%), a similar ΔTB vs. TPW behavior exists

(Figure 9, top-right panel) to what was found over land for $TPW > 5 \text{ kg}\cdot\text{m}^{-2}$ (the same value was found in the regression tree analysis). SCT shows always lower 166 ΔTB than for CS, meaning that the presence of supercooled water droplets on top of the cloud attenuates the polarization signal by the surface also for very low TPW. However, the positive trend of ΔTB with SWP (Figure 9, bottom-right panel) is evident only for $SWP < 0.04 \text{ kg}\cdot\text{m}^{-2}$. Moreover, the presence of supercooled droplets on top of the cloud reduces this positive trend and shows ΔTB (median values) lower than without supercooled droplets (SN) by 1–2 K (40%). When the supercooled droplets are embedded in the cloud, the trend of ΔTB is similar to the snowfall only case (similarly to what found over land).

The significance of the results shown in Figure 9 was also tested by carrying out a statistical test on the Spearman correlation coefficient between 166 ΔTB and SWP, for each manifold, similar to what was done for the results in Figure 8. The test confirmed that the positive trends shown in Figure 9 are significant and represent the trends between the two variables in each manifold, while no trend was evidenced for SCT over sea ice.

4. Discussion

This study represents the first attempt to analyze in detail the GMI high-frequency channel response, and in particular the 166 GHz V-pol and H-pol channels, to snowfall using CloudSat CPR as a reference. The analysis has been carried out first considering three case studies, and highlighting very important aspects in the behavior of TBs and ΔTB s for the 166 GHz and 183.3 GHz channels under different conditions. Then the analysis of the whole GMI-CPR snowfall dataset allowed identifying quantitatively environmental conditions and cloud properties where 166 ΔTB shows sensitivity to snowfall (detection and amount). Finally, we outlined the complex interconnections between 166 ΔTB and TB with surface type, TPW, SWP, and the presence and vertical distribution of supercooled droplets.

Recent studies using GMI and DPR have highlighted the crucial role of high-frequency channels for snowfall monitoring using microwave radiometer observations [2,18]. This study is complementary to that of Ebtehaj and Kummerow [18] because it also analyzes in detail the GMI high-frequency channel response to snowfall, but uses CloudSat, instead of DPR, observations as a valuable surface snowfall reference. This study therefore focuses on higher latitude snowfall systems because most of the GMI-CPR coincidences occur around 60°N/S , and it includes very weak and/or shallow snowfall systems that are not considered in the study by Ebtehaj and Kummerow [18] where DPR was used as reference (and therefore, mostly based on more intense snowfall systems). Indeed, as shown in Casella et al. [28], DPR detects 5–7% of the global snowfall events with respect to CloudSat, while 29–34% of the global snowfall mass is correctly detected by DPR v4 products. This study also analyzes the behavior of 166 ΔTB (and 183 ΔTB for the case studies) associated with CloudSat-detected snowfall events, following Gong and Wu [25] who analyze global 166 ΔTB signature and find that at higher latitudes the relationship with precipitation is quite complex and requires a dedicated analysis.

The case studies and the regression tree analysis both illustrate that TPW and surface type are fundamental parameters needed to determine to what extent GMI TB behavior is related to snowfall. The regression tree analysis was specifically carried out to find hierarchically environmental variables and cloud properties that had the largest impact on the 166 ΔTB variability, and analyze the sensitivity of 166 ΔTB to snowfall occurrence and amount for the different regimes identified by the tree. The analysis confirmed what was evidenced from the case studies, finding that the surface type and TPW are the two most important parameters to consider to be able to correctly interpret 166 ΔTB . Over land, 166 ΔTB can be a useful parameter to identify snowfall only in moist conditions ($TPW > 3.6 \text{ kg}\cdot\text{m}^{-2}$) and for moderate to heavy snowfall amounts ($IWP > 0.24 \text{ kg}\cdot\text{m}^{-2}$). A similar behavior was found over sea ice ($SIC > 57\%$), where, for $TPW > 5.1 \text{ kg}\cdot\text{m}^{-2}$, 166 ΔTB always shows a good correlation with SWP, while over open water (or $SIC < 57\%$) the polarization due to the surface masks any signal related to the snowfall.

A further step to define the conditions for the sensitivity of ΔTB and TBs at 166 GHz to snowfall has been carried out analogously to Gong and Wu [25], but exploiting the GMI-CPR coincidence

dataset available mostly at latitudes around 60°N/S. The behavior of ΔTB vs. TB at 166 GHz for the whole dataset, differently from what was found by Gong and Wu [25], evidenced the strong surface/atmosphere contribution to the signal in presence of snowfall because of the lower water vapor contents in winter atmospheres at higher latitudes in the GMI-CPR snowfall dataset compared to the global GMI-DPR dataset used by Gong and Wu [25]. A very distinct behavior of ΔTB -TB relation has been found for the three different surface types: land, open water, and sea ice. The analysis confirmed what was found by the regression tree, showing that over land and over sea ice, and for $TPW > 3\text{--}4 \text{ kg}\cdot\text{m}^{-2}$ and $TPW > 5 \text{ kg}\cdot\text{m}^{-2}$, respectively, 166 ΔTB can provide valuable information for snowfall detection and retrieval, while, over open water (or low SIC), it is dominated by the polarization by the surface. However, over open water (and to less extent over sea ice), TBs at 166 GHz show a strong dependence on SWP mostly in presence of intense snowfall events and moist conditions ($SWP > 0.5 \text{ kg}\cdot\text{m}^{-2}$, and $TPW > 10 \text{ kg}\cdot\text{m}^{-2}$).

Finally, an analysis of the effect of supercooled water layers on the 166 GHz TBs and ΔTB was undertaken. Our results confirm what was evidenced by Ebtehaj and Kummerow [18] for snow cover cases during winter. They found that in very cold and dry conditions, with a radiatively cold background surface (i.e., snow-covered land), in presence of snowfall it is possible to have an increase of TBs. Previous studies on ground-based measurements [19,20] showed that TB enhancement can occur in presence of snowfall, and that high SWP enhances polarization differences at 150 GHz, while the presence of supercooled water damps the polarization differences. Our results show that such an increase may be related to the presence of supercooled droplets, as over land TBs can be up to 10 K higher than snow-only cases because of the supercooled water droplet emission. This effect is also stronger when the droplets are found on top of the ice cloud. In the presence of supercooled droplets, 166 GHz TBs therefore do not show a significant trend with the SWP because the cloud droplet emission compensates for the scattering effects by the ice cloud. Similar behavior is observed over sea ice. This effect is noticeable in very dry conditions ($TPW < 5 \text{ kg}\cdot\text{m}^{-2}$). However, 166 ΔTB over land (and sea ice) shows a very distinct trend in presence of snowfall, increasing as SWP increases (for $TPW > 3.5 \text{ kg}\cdot\text{m}^{-2}$ over land and for $TPW > 5 \text{ kg}\cdot\text{m}^{-2}$ over sea ice). Moreover, over land the depolarization effect at 166 GHz induced by the cloud droplets is on average not enough to eliminate this trend. This shows that ΔTB can be a very valuable parameter to use for snowfall detection for the following difficult circumstances: (1) over land (to a less extent over sea ice); (2) for very weak snowfall events (very low SWP); and (3) for low TPW values in $4\text{--}5 \text{ kg}\cdot\text{m}^{-2}$ range (consistently to what found in the regression tree analysis).

A few distinct scenarios governed by ambient TPW values were delineated by both analyzing case studies and the entire combined GPM-CPR snowfall dataset. First, when TPW values are elevated ($>10 \text{ kg}\cdot\text{m}^{-2}$), only the deeper and more intense snow-producing clouds (e.g., 0–10 dBZ between 6 and 8 km altitude) can produce a significant signal at high frequencies. This is because, as TPW increases, the signal from the cold surface becomes negligible, the weighting function peaks at higher levels, and therefore only thicker clouds (6–8 km) can impact the TBs. Under such circumstances, there is an evident scattering signal at high frequencies (lower 166 GHz and 183.3 GHz TB values with respect to the atmospheric/surface contribution) with a significant 166 GHz polarization signal also visible (i.e., 166 ΔTB increases). This behavior relates to the spring season findings by Ebtehaj and Kummerow [18] (presumably characterized by higher TPW), when the atmospheric contribution due to the water vapor is significant, the surface is radiatively warmer, and the snowfall is associated with a high-frequency (166 GHz and 183.3 GHz) TB decrease due to scattering. The presence of supercooled cloud droplets, however, further complicates matters that may hamper the GMI ability to detect snowfall. Shallower clouds ($<5 \text{ km}$ cloud top height) do not possess a significant 166 GHz or 183.3 GHz signal. The supercooled cloud droplet emission signal (where present) can be quite significant at 89 GHz, while it is masked by the water vapor contribution at 166 GHz.

For lower TPW values ($5 \text{ kg}\cdot\text{m}^{-2} < TPW < 10 \text{ kg}\cdot\text{m}^{-2}$), the high-frequency TB scattering effect is visible for the most intense ($Z > 5 \text{ dBZ}$) and deeper clouds (6–8 km), even in the presence of a

radiatively cold surface background. The 166 Δ TB over land and sea ice can become quite significant in presence of snowfall (>10 K). This signal is often more evident than the single frequency scattering signal. As TPW decreases further until a $1 \text{ kg}\cdot\text{m}^{-2}$ threshold (snowfall events are extremely rare under this TPW value), the signal from shallower or less intense clouds becomes visible at high GMI frequencies. In the presence of a cold surface background, TBs typically increase with respect to the clear sky, where TBs mainly respond to the radiatively cold snow cover and low emission by water vapor. Such TB increases can be quite significant at 89 GHz, but are less evident at 166 GHz (H-pol channels also display an enhanced signal because the surface emissivity is lower). Once again, these trends relate to the findings by Ebtehaj and Kummerow [18] that show a TB increase at all frequencies over radiatively cold backgrounds (snow cover) for winter snowfall cases. However, as shown by complementary CALIPSO cloud phase products, such warm/cold contrast of the cloud with respect to the surface is also due to the presence of supercooled droplets.

It is worth noting that, except for the case study discussion, the results presented in this study are based on the analysis under the condition that surface snowfall is occurring ($2\text{C-SNOW SWP} > 0 \text{ kg}\cdot\text{m}^{-2}$), and these are compared to cases where surface snowfall is not occurring ($2\text{C-SNOW SWP} = 0 \text{ kg}\cdot\text{m}^{-2}$) which include upper level ice clouds with no snowfall at the surface (according to 2C-SNOW product). A separate analysis of the Δ TB and TB sensitivity to ice clouds (with no snowfall at the surface) should be carried out to optimally exploit the results of this study towards the development of a snowfall detection algorithm.

5. Conclusions and Future Work

Three related analyses on the sensitivity of GMI high-frequency channels to snowfall, at higher latitudes (mostly around 60°N/S), using coincident CloudSat CPR (and CALIPSO) observations were performed in this study:

1. A snowfall case study analysis;
2. A regression tree statistical analysis applied to the entire GMI-CPR snowfall dataset illustrating 166 GHz Δ TB polarization signal variability related to various parameters and associated snowfall detection efficacy applications; and
3. A 166 GHz Δ TB, TB, and snow water path relationship analysis for various surface types and highlighting supercooled water layer effects.

The case studies have evidenced qualitatively the important combined role of background surface characteristics, atmospheric water vapor content and presence and vertical distribution of supercooled cloud water, on the high-frequency signal associated with different snow-producing clouds and SWP amounts. The regression tree analysis has contributed to quantitatively define critical thresholds of various parameters (e.g., SIC, TPW, and SWP) for the potential use of the 166 GHz polarization difference for snowfall detection over land and over sea. The combined 166 GHz Δ TB and TB analysis, based on the significant surface types and environmental variables identified by the regression tree, has contributed to define the conditions and the potentials of the 166 GHz channel in relation to snowfall at latitudes around 60°N/S , and has quantitatively demonstrated the augmented complexity of such relations in presence of supercooled cloud droplets. It is important to consider that the most accurate and up to date CloudSat/CALIPSO/ECMWF snowfall-related products have been used in this study. These products are subject to uncertainties whose assessments are worthy of separate exhaustive investigations. However, based on previous work and a critical analysis of our results, we deem that these uncertainties are limited enough to obtain meaningful insights from the study shown.

The analyses presented in this paper demonstrate the great potential of the combined GMI and CloudSat observational dataset to define microwave radiometer snowfall detection limitations and capabilities, in relation to key environmental characteristics (i.e., background surface, SIC and TPW). All components of this study ultimately improve our ability to interpret GMI observations associated with a diverse set of snowfall events comprised of different cloud microphysical and macrophysical

properties and associated with varying environmental conditions. Future work will leverage the current findings through many possible research pathways. First, actual CloudSat and GMI GPROF retrievals will be analyzed to investigate GMI snowfall retrieval strengths and shortcomings, and offer possible solutions to mitigate systematic GPROF snowfall retrieval deficiencies. Second, future work will be dedicated to illustrating the inherent value of using GMI channels at the time of the observation to properly characterize the frozen background surface (both SIC and snow cover). Third, this study will be extended to other radiometers (i.e., ATMS) with different high microwave frequency channel availability, viewing geometry and spatial resolution, but with high latitude coverage.

This study aims at defining some quantitative criteria and guidelines to build a GMI snowfall detection algorithm based on CloudSat. Important caveats are highlighted for future algorithm development where 166 GHz scattering and polarization signals might be exploited for surface snowfall retrievals. To this purpose, further analysis on the sensitivity of GMI channels to ice clouds (without snowfall at the surface) should be carried out. The algorithm will need to characterize the extremely variable background surface for each GMI pixel at the time of the overpass because at high latitudes (especially in cold and dry conditions), high-frequency channels may be affected by the emission and polarization signal from the surface. Low frequency channels can be effectively used to infer information about the background surface (e.g., sea ice concentration, ground, and water). Atmospheric water vapor content is also a fundamental variable for determining the atmospheric contribution to the upwelling radiation at the time of the overpass, and for defining to what extent high-frequency channel scattering and polarization signal can be related to snowfall. This algorithm framework will provide improved snowfall detection capabilities to enhance future high-latitude PMW precipitation estimates.

Acknowledgments: This study has been conducted within the EUMETSAT “Satellite Application Facility on Support to Operational Hydrology and Water Management” (H SAF) Federated Activity H_SAF_FA15_01 “Cooperation on the use of combined spaceborne active and passive microwave observations for precipitation retrieval”. This work was supported by the EUMETSAT H SAF (CDOP-2 and H_SAF_FA15_01), the Earth2Observe “Global Earth Observation for Integrated Water 16 Resource Assessment” project funded under the EU DG Research 7th Framework Programme 17 (FP7). Daniele Casella was at CNR-ISAC until December 2016, partly supported by the EUMETSAT H-SAF, and by the CNR Short Term Mobility Program 2015. Partial support for Anna Cinzia Marra from the Italian Research Project of National Interest 2015 (PRIN 2015) 4WX5NA, and for Mark Kulie from NASA research grants NNX16AE21G and NNX14AB22G, and from the CNR Short Term Mobility Program 2016 are also gratefully acknowledged. The datasets used in this study have been collected from the NASA PPS website [48] (GPM products, 2B-CSATGPM product), from the CloudSat website [49] (CPR products), from DARDAR product [50], and from AMSR2 sea ice dataset [51]. The H SAF Science Management, in particular Capt. Davide Melfi and Stefano Dietrich, is warmly acknowledged for supporting the Federated Activity H_SAF_FA15_01. The PMM Research Program and EUMETSAT are acknowledged for supporting H SAF and GPM collaboration through the approval of the no-cost H SAF-GPM proposal “H SAF and GPM: precipitation algorithm development and validation activity”. The authors want to sincerely express their gratitude to the two anonymous reviewers for their useful comments and suggestions, to Joe Turk for developing and sharing the 2B-CSATGPM dataset used in this study, and to Norm Wood for the valuable discussions and suggestions on the use of the CloudSat 2C-SNOW-profile product.

Author Contributions: Giulia Panegrossi, Daniele Casella and Mark Kulie conceived and designed the work; Daniele Casella contributed to create the dataset; Jean-François Rysman contributed to create the dataset and created original analysis tools; Anna Cinzia Marra and Paolo Sanò contributed to the analysis tools; and Giulia Panegrossi, Mark Kulie and Jean-François Rysman wrote the paper. All co-authors have contributed to the group discussions on the results, and to the final draft.

Conflicts of Interest: The authors declare no conflict of interest. The funding sponsors had no role in the design of the study; in the collection, analyses, or interpretation of data; in the writing of the manuscript, and in the decision to publish the results.

References

1. Skofronick-Jackson, G.; Johnson, B.T. Surface and atmospheric contributions to passive microwave brightness temperatures for falling snow events. *J. Geophys. Res.* **2011**, *116*. [[CrossRef](#)]
2. You, Y.; Wang, N.-Y.; Ferraro, R.; Rudlosky, S. Quantifying the Snowfall Detection Performance of the GPM Microwave Imager Channels over Land. *J. Hydrometeorol.* **2017**, *18*, 729–751. [[CrossRef](#)]
3. Kulie, M.S.; Bennartz, R.; Greenwald, T.J.; Chen, Y.; Weng, F. Uncertainties in Microwave Properties of Frozen Precipitation: Implications for Remote Sensing and Data Assimilation. *J. Atmos. Sci.* **2010**, *67*, 3471–3487. [[CrossRef](#)]
4. Prigent, C.; Aires, F.; Rossow, W.B. Land Surface Microwave Emissivities over the Globe for a Decade. *Bull. Am. Meteorol. Soc.* **2006**, *87*, 1573–1584. [[CrossRef](#)]
5. Turk, F.J.; Haddad, Z.S.; You, Y. Principal Components of Multifrequency Microwave Land Surface Emissivities. Part I: Estimation under Clear and Precipitating Conditions. *J. Hydrometeorol.* **2014**, *15*, 3–19. [[CrossRef](#)]
6. Kongoli, C.; Meng, H.; Dong, J.; Ferraro, R. A snowfall detection algorithm over land utilizing high-frequency passive microwave measurements—Application to ATMS: A Snowfall Detection Algorithm over Land. *J. Geophys. Res. Atmos.* **2015**, *120*, 1918–1932. [[CrossRef](#)]
7. Liu, G. Deriving snow cloud characteristics from CloudSat observations. *J. Geophys. Res.* **2008**, *113*. [[CrossRef](#)]
8. Kulie, M.S.; Bennartz, R. Utilizing Spaceborne Radars to Retrieve Dry Snowfall. *J. Appl. Meteorol. Climatol.* **2009**, *48*, 2564–2580. [[CrossRef](#)]
9. Kulie, M.S.; Milani, L.; Wood, N.B.; Tushaus, S.A.; Bennartz, R.; L'Ecuyer, T.S. A Shallow Cumuliform Snowfall Census Using Spaceborne Radar. *J. Hydrometeorol.* **2016**, *17*, 1261–1279. [[CrossRef](#)]
10. Spencer, R.W.; Goodman, H.M.; Hood, R.E. Precipitation Retrieval over Land and Ocean with the SSM/I: Identification and Characteristics of the Scattering Signal. *J. Atmos. Ocean. Technol.* **1989**, *6*, 254–273. [[CrossRef](#)]
11. Bennartz, R.; Petty, G.W. The Sensitivity of Microwave Remote Sensing Observations of Precipitation to Ice Particle Size Distributions. *J. Appl. Meteorol.* **2001**, *40*, 345–364. [[CrossRef](#)]
12. Petty, G.W. Physical retrievals of over-ocean rain rate from multichannel microwave imagery. Part I: Theoretical characteristics of normalized polarization and scattering indices. *Meteorol. Atmos. Phys.* **1994**, *54*, 79–99. [[CrossRef](#)]
13. Kuo, K.-S.; Olson, W.S.; Johnson, B.T.; Grecu, M.; Tian, L.; Clune, T.L.; van Aartsen, B.H.; Heymsfield, A.J.; Liao, L.; Meneghini, R. The Microwave Radiative Properties of Falling Snow Derived from Nonspherical Ice Particle Models. Part I: An Extensive Database of Simulated Pristine Crystals and Aggregate Particles, and Their Scattering Properties. *J. Appl. Meteorol. Climatol.* **2016**, *55*, 691–708. [[CrossRef](#)]
14. Olson, W.S.; Tian, L.; Grecu, M.; Kuo, K.-S.; Johnson, B.T.; Heymsfield, A.J.; Bansemmer, A.; Heymsfield, G.M.; Wang, J.R.; Meneghini, R. The Microwave Radiative Properties of Falling Snow Derived from Nonspherical Ice Particle Models. Part II: Initial Testing Using Radar, Radiometer and In Situ Observations. *J. Appl. Meteorol. Climatol.* **2016**, *55*, 709–722. [[CrossRef](#)]
15. Skofronick-Jackson, G.M.; Kim, M.-J.; Weinman, J.A.; Chang, D.-E. A physical model to determine snowfall over land by microwave radiometry. *IEEE Trans. Geosci. Remote Sens.* **2004**, *42*, 1047–1058. [[CrossRef](#)]
16. Bennartz, R.; Bauer, P. Sensitivity of microwave radiances at 85–183 GHz to precipitating ice particles. *Radio Sci.* **2003**, *38*. [[CrossRef](#)]
17. Di Michele, S.; Bauer, P. Passive microwave radiometer channel selection based on cloud and precipitation information content. *Q. J. R. Meteorol. Soc.* **2006**, *132*, 1299–1323. [[CrossRef](#)]
18. Ebtehaj, A.M.; Kummerow, C.D. Microwave retrievals of terrestrial precipitation over snow-covered surfaces: A lesson from the GPM satellite. *Geophys. Res. Lett.* **2017**, *44*, 6154–6162. [[CrossRef](#)]
19. Kneifel, S.; Löhnert, U.; Battaglia, A.; Crewell, S.; Siebler, D. Snow scattering signals in ground-based passive microwave radiometer measurements. *J. Geophys. Res.* **2010**, *115*. [[CrossRef](#)]
20. Xie, X.; Löhnert, U.; Kneifel, S.; Crewell, S. Snow particle orientation observed by ground-based microwave radiometry. *J. Geophys. Res. Atmos.* **2012**, *117*. [[CrossRef](#)]
21. Kongoli, C.; Pellegrino, P.; Ferraro, R.R.; Grody, N.C.; Meng, H. A new snowfall detection algorithm over land using measurements from the Advanced Microwave Sounding Unit (AMSU). *Geophys. Res. Lett.* **2003**, *30*. [[CrossRef](#)]

22. Surussavadee, C.; Staelin, D.H. Satellite Retrievals of Arctic and Equatorial Rain and Snowfall Rates Using Millimeter Wavelengths. *IEEE Trans. Geosci. Remote Sens.* **2009**, *47*, 3697–3707. [[CrossRef](#)]
23. Noh, Y.-J.; Liu, G.; Jones, A.S.; Vonder Haar, T.H. Toward snowfall retrieval over land by combining satellite and in situ measurements. *J. Geophys. Res.* **2009**, *114*. [[CrossRef](#)]
24. Kummerow, C.D.; Randel, D.L.; Kulie, M.; Wang, N.-Y.; Ferraro, R.; Joseph Munchak, S.; Petkovic, V. The Evolution of the Goddard Profiling Algorithm to a Fully Parametric Scheme. *J. Atmos. Ocean. Technol.* **2015**, *32*, 2265–2280. [[CrossRef](#)]
25. Gong, J.; Wu, D.L. Microphysical properties of frozen particles inferred from Global Precipitation Measurement (GPM) Microwave Imager (GMI) polarimetric measurements. *Atmos. Chem. Phys.* **2017**, *17*, 2741–2757. [[CrossRef](#)]
26. Boening, C.; Lebsack, M.; Landerer, F.; Stephens, G. Snowfall-driven mass change on the East Antarctic ice sheet. *Geophys. Res. Lett.* **2012**, *39*. [[CrossRef](#)]
27. Behrangi, A.; Christensen, M.; Richardson, M.; Lebsack, M.; Stephens, G.; Huffman, G.J.; Bolvin, D.; Adler, R.F.; Gardner, A.; Lambriksen, B.; et al. Status of high-latitude precipitation estimates from observations and reanalyses. *J. Geophys. Res. Atmos.* **2016**, *121*, 4468–4486. [[CrossRef](#)]
28. Casella, D.; Panegrossi, G.; Sanò, P.; Marra, A.C.; Dietrich, S.; Johnson, B.T.; Kulie, M.S. Evaluation of the GPM-DPR snowfall detection capability: Comparison with CloudSat-CPR. *Atmos. Res.* **2017**, *197*, 64–75. [[CrossRef](#)]
29. L'Ecuyer, T.S.; Jiang, J.H. Touring the atmosphere aboard the A-Train. *Phys. Today* **2010**, *63*, 36–41. [[CrossRef](#)]
30. Palerme, C.; Kay, J.E.; Genthon, C.; L'Ecuyer, T.; Wood, N.B.; Claud, C. How much snow falls on the Antarctic ice sheet? *Cryosphere* **2014**, *8*, 1577–1587. [[CrossRef](#)]
31. Wang, Y.; Liu, G.; Seo, E.-K.; Fu, Y. Liquid water in snowing clouds: Implications for satellite remote sensing of snowfall. *Atmos. Res.* **2013**, *131*, 60–72. [[CrossRef](#)]
32. Milani, L.; Kulie, M.S.; Casella, D.; Dietrich, S.; L'Ecuyer, T.S.; Panegrossi, G.; Porcù, F.; Sanò, P.; Wood, N.B. CloudSat Snowfall Estimates over Antarctica and the Southern Ocean: An Assessment of Independent Retrieval Methodologies and Multi-Year Snowfall Analysis. *Atmos. Res.* **2017**. under review.
33. Turk, F.J. CloudSat-GPM Coincidence Dataset. 2016. Available online: https://pmm.nasa.gov/sites/default/files/document_files/CSATGPM_COIN_ATBD.pdf (accessed on 4 December 2017).
34. Grecu, M.; Olson, W.S.; Munchak, S.J.; Ringerud, S.; Liao, L.; Haddad, Z.; Kelley, B.L.; McLaughlin, S.F. The GPM Combined Algorithm. *J. Atmos. Ocean. Technol.* **2016**, *33*, 2225–2245. [[CrossRef](#)]
35. Iguchi, T.; Seto, S.; Meneghini, R.; Yoshida, N.; Awaka, J.; Kubota, T. GPM/DPR Level-2 Algorithm Theoretical Basis Document. 2016. Available online: http://www.eorc.jaxa.jp/GPM/doc/algorithm/ATBD_DPR_2015_whole_2a.pdf (accessed on 4 December 2017).
36. Wood, N.B.; L'Ecuyer, T.S.; Bliven, F.L.; Stephens, G.L. Characterization of video disdrometer uncertainties and impacts on estimates of snowfall rate and radar reflectivity. *Atmos. Meas. Tech.* **2013**, *6*, 3635–3648. [[CrossRef](#)]
37. Wood, N.B.; L'Ecuyer, T.S.; Heymsfield, A.J.; Stephens, G.L.; Hudak, D.R.; Rodriguez, P. Estimating snow microphysical properties using collocated multisensor observations. *J. Geophys. Res. Atmos.* **2014**, *119*, 8941–8961. [[CrossRef](#)]
38. Hiley, M.J.; Kulie, M.S.; Bennartz, R. Uncertainty analysis for CloudSat snowfall retrievals. *J. Appl. Meteorol. Climatol.* **2011**, *50*, 399–418. [[CrossRef](#)]
39. Chen, S.; Hong, Y.; Kulie, M.; Behrangi, A.; Stepanian, P.M.; Cao, Q.; You, Y.; Zhang, J.; Hu, J.; Zhang, X. Comparison of snowfall estimates from the NASA CloudSat Cloud Profiling Radar and NOAA/NSSL Multi-Radar Multi-Sensor System. *J. Hydrol.* **2016**, *3644*. [[CrossRef](#)]
40. Delanoë, J.; Hogan, R.J. A variational scheme for retrieving ice cloud properties from combined radar, lidar, and infrared radiometer. *J. Geophys. Res.* **2008**, *113*. [[CrossRef](#)]
41. Delanoë, J.; Hogan, R.J. Combined CloudSat-CALIPSO-MODIS retrievals of the properties of ice clouds. *J. Geophys. Res.* **2010**, *115*. [[CrossRef](#)]
42. Hall, D.K.; Riggs, G.A.; Salomonson, V.V.; DiGirolamo, N.E.; Bayr, K.J. MODIS snow-cover products. *Remote Sens. Environ.* **2002**, *83*, 181–194. [[CrossRef](#)]
43. Spreen, G.; Kaleschke, L.; Heygster, G. Sea ice remote sensing using AMSR-E 89-GHz channels. *J. Geophys. Res.* **2008**, *113*. [[CrossRef](#)]

44. Liu, G.; Seo, E.-K. Detecting snowfall over land by satellite high-frequency microwave observations: The lack of scattering signature and a statistical approach. *J. Geophys. Res. Atmos.* **2013**, *118*, 1376–1387. [[CrossRef](#)]
45. Breiman, L.; Friedman, J.H.; Olshen, R.A.; Stone, C.J. *Classification and Regression Trees*; Chapman & Hall/CRC: Boca Raton, FL, USA, 1984; p. 368.
46. Therneau, T.M.; Atkinson, E.J. *An Introduction to Recursive Partitioning Using the Rpart Routines*; Mayo Clinic: Rochester, MN, USA, 1997; p. 452.
47. Ceccaldi, M.; Delanoë, J.; Hogan, R.J.; Pounder, N.L.; Protat, A.; Pelon, J. From CloudSat-CALIPSO to EarthCare: Evolution of the DARDAR cloud classification and its comparison to airborne radar-lidar observations. *J. Geophys. Res. Atmos.* **2013**, *118*, 7962–7981. [[CrossRef](#)]
48. NASA Precipitation Processing System. 2017. Available online: <ftp://arthurhou.pps.eosdis.nasa.gov> (accessed on 12 October 2017).
49. CloudSat Product Website. 2017. Available online: <ftp.cloudsat.cira.colostate.edu> (accessed on 12 October 2017).
50. DARDAR Product Website. 2016. Available online: <http://www.icare.univ-lille1.fr/projects/dardar> (accessed on 12 October 2017).
51. AMSR2 Sea Ice Dataset. 2017. Available online: <https://seaice.uni-bremen.de/sea-ice-concentration/> (accessed on 12 October 2017).



© 2017 by the authors. Licensee MDPI, Basel, Switzerland. This article is an open access article distributed under the terms and conditions of the Creative Commons Attribution (CC BY) license (<http://creativecommons.org/licenses/by/4.0/>).